Optomechanical second-order sidebands and group delays in a spinning resonator with a parametric amplifier and non-Markovian effects

W. Zhang[1] and H. Z. Shen[1,2,*]

[1]*Center for Quantum Sciences and School of Physics, Northeast Normal University, Changchun 130024, China*

[2]*Center for Advanced Optoelectronic Functional Materials Research and Key Laboratory for UV Light-Emitting Materials and Technology of Ministry of Education, Northeast Normal University, Changchun 130024, China*

(Received 3 May 2023; revised 21 December 2023; accepted 12 February 2024; published 1 March 2024)

We investigate the generation of the frequency components at the second-order sidebands based on a spinning resonator containing a degenerate optical parametric amplifier (OPA). We show that an OPA driven by different pumping frequencies inside a cavity can enhance and modulate the amplitude of the second-order sideband with different influences. We find that both the second-order sideband amplitude and its associated group delay sensitively depend on the nonlinear gain of the OPA, the phase of the field driving the OPA, the rotation speed of the resonator, and the incident direction of the input fields. Tuning the pumping frequency of the OPA can remain the localization of the maximum value of the sideband efficiency and nonreciprocal behavior due to the optical Sagnac effect, which also can adjust the linewidth of the suppressive window of the second-order sideband. Furthermore, we extend the study of the second-order sideband to the non-Markovian bath, which consists of a collection of infinite oscillators (bosonic photonic modes). We illustrate that the second-order sidebands in a spinning resonator exhibit a transition from the non-Markovian to the Markovian regime by controlling the environmental spectral width. We also study the influences of the decay from the non-Markovian environment coupling to an external reservoir on the efficiency of second-order upper sidebands. This indicates a promising way to enhance or steer optomechanically induced transparency devices in nonlinear optical cavities and provides potential applications for precision measurement, optical communications, and quantum sensing.

DOI: 10.1103/PhysRevA.109.033701

I. INTRODUCTION

In recent years, much attention has been paid to the field of optomechanics [1–5], in which considerably different phenomena have been encountered. There are different applications such as cooling of a mechanical resonator [6–10], gravitational wave detection [11–13], optical bistability [14–16], optomechanical mass sensors [17], quantum measurement [18], and detection of weak microwave signals [19–21] in merged quantum-mechanical systems with nano- and micromechanics. A recent advance closely related to the present study is optomechanically induced transparency (OMIT) [22–26]. In OMIT, the intense red-detuned optical control field produces anti-Stokes scattering, which alters the optical response of the optomechanical cavity, making it transparent in a narrow bandwidth around the cavity resonance for a probe beam [27]. As an analog of electromagnetically induced transparency [28,29], OMIT plays an essential role in optical storage and optical telecommunication [30–33]. In the past several years, primary advancements have concentrated on the linearization of the optomechanical interaction, where we properly explain OMIT by linearizing the optomechanical interaction while ignoring the intrinsic nonlinear nature of the optomechanical coupling [29,34]. In recent years, it has been found that nonlinear optical interactions in materials can increase the photons circulating in microcavities, such as parametric amplification and the optical Kerr effect [35–38], which has emerged as an important new frontier in cavity optomechanics. In the classical mechanism, nonlinear optomechanical interaction brings about unconventional photon blockade [39–41], optomechanical chaos [42], and sideband generation [43].

Nonreciprocal transmission plays a very important role in the process of quantum information [44–47] due to the characteristics of unidirectional transmission. The nonreciprocal transmission of the optical signal allows the flow of light from one side but blocks it from the other, which resembles the traditional semiconductor $p-n$ junction. Recently, OMIT has been demonstrated in a rotating optomechanical system with a whispering-gallery-mode microresonator [48–50]. The experiment [51] showed that optical nonreciprocal devices can be achieved by spinning an optomechanical resonator. In such a spinning resonator, due to the Sagnac effect, the frequencies of the clockwise and counterclockwise modes experience Sagnac-Fizeau shifts. Additionally, it also suggested a new scheme to achieve optical nonreciprocity wherein the optical sidebands strongly rely on the rotary direction of the resonator, which is different from what the nonlinearity-based schemes demonstrated [52–56]. The spinning resonator systems have developed rapidly, including nanoparticle sensing [57], mass sensing [58], nonreciprocal photon blockades [59,60], nonreciprocal phonon lasers [61], unidirectional signal amplification [62], breaking anti-parity-time symmetry [63], and optical solitons [64].

*Corresponding author: shenhz458@nenu.edu.cn

It has been shown that combining nonlinear optics and optomechanics has resulted in many kinds of physical phenomena to enhance quantum effects [65,66]. An optical parametric amplifier (OPA) inside the optomechanical cavity, which is pumped by an external laser, can directly lead to optical amplification and modulate the optomechanical coupling in a way analogous to periodic cavity driving [67–69]. The OPA is able to generate pairs of down-converted photons, which shows nearly perfect single or dual squeezing. Therefore, the OPA can modify the dynamical instabilities and nonlinear dynamics of the system [70–72]. Numerous applications have been studied owing to these features, such as the realization of strong mechanical squeezing [73], enhancing optomechanical cooling [74], the normal-mode splitting [75], controlling the photon blockade [76–78], and the increase of atom-cavity coupling [79].

Recently, studying the nonlinear optomechanical interactions in the presence of a coherent mechanical pump has emerged as an important frontier [80–83]. Due to the existence of nonlinear optomechanical interactions, second-order and higher-order sidebands have been generated in optomechanical systems [43,84–88]. Generation of spectral components at high-order OMIT sidebands has been demonstrated analytically, which may have great potential in precise sensing of charges [89,90], phonon number [91], weak forces [92,93], single-particle detection [94], magnetometer [95], mass sensor [96,97], and high-order squeezed frequency combs [98]. However, actually, high-order OMIT sidebands are generally much weaker than the probe signal, which imposes many difficulties in detecting and utilizing the second-order sideband. Therefore, the enhancement and control of second-order sidebands have attracted much interest. Moreover, by controlling the group delay of the output light field, which is caused by rapid phase dispersion, slow light or fast light effects can be achieved [48,99–104]. The fast and slow light effects of the optomechanical system have a wide range of applications in optical communications and interferometry [105,106]. The hybrid nonlinear optomechanical system provides an important platform for further study of the tunable slow and fast effects.

For open systems [107,108], only if the coupling between the system and environment is weak, where the characteristic times of the bath are sufficiently smaller than those of the quantum system under study, is the Markovian approximation valid. This means that the Markovian approximation may fail in some cases, e.g., two-state systems, harmonic oscillators, coupled cavities, etc. [109–137], where we need to consider the influences of non-Markovian effects on the system dynamics. Moreover, we show that the non-Markovian process proves to be useful in quantum information processing including quantum state engineering, quantum control, and quantum channel capacity [138–142] and has been realized in experiment [143–158].

The above considerations motivate us to explore how to enhance and control the second-order OMIT sidebands and group delays in a spinning resonator with a parametric amplifier and non-Markovian effects.

In this paper we consider the influence of the OPA driven with different pumping frequencies on the second-order sideband generation in a rotating optomechanical system, which is coherently driven by a control field and a probe field. The results show that the second-order sidebands in the rotating resonator can be greatly enhanced in the presence of the OPA while maintaining the nonreciprocal behavior due to the optical Sagnac effect. The second-order sidebands can be adjusted simultaneously by the pumping frequency and phase of the field driving the OPA, the gain coefficient of the OPA, the rotation speed of the resonator, and the incident direction of the input fields. We compare the differences in efficiency of the second-order sideband generation when the OPA is driven by different pumping frequencies. Due to the Sagnac transformation and the presence of the OPA, we find that the group delay of the second-order upper sideband can be tuned by adjusting the nonlinear gain and phase of the field driving the OPA, the rotation speed of the resonator, and the incident direction of the input fields in the spinning optomechanical system. The second-order OMIT sidebands in the spinning resonator are then generalized to the non-Markovian regimes and compared with the Markovian approximation in the wideband limit. The influence of the decay from the non-Markovian environment coupling to an external reservoir on the efficiency of second-order upper sidebands is also investigated. Our paper indicates an advantage of using a hybrid nonlinear system, which provides an effective way to further control and enhance second-order and higher-order sidebands in a nonreciprocal optical device.

The rest of this paper is organized as follows. In Sec. II we give the efficiency of the second-order sideband and its group delay by solving the Heisenberg-Langevin equations. In Sec. III we discuss the influence of the OPA excited by a pump driving with the frequency being the sum of the frequencies of the strong control field and the weak probe field driving the resonator on the second-order upper and lower sidebands generation in the spinning resonator. In Sec. IV we study the group delay of the second-order upper sideband. In Sec. V we show the influence of the OPA on the second-order sideband generation when the OPA is excited by a pump driving with the frequency setting to twice the frequency of the strong control field. In Sec. VI we extend nonreciprocal second-order sidebands in the spinning resonator to a non-Markovian bath and compare it with that in the Markovian regime. Moreover, we also study the influence of the decay from the non-Markovian environment coupling to an external reservoir on the efficiency of second-order upper sidebands. Section VII summarizes our work and discusses the conclusions.

II. MODEL

As schematically shown in Figs. 1(a) and 1(b), the model we consider is a rotating whispering-gallery-mode microresonator (containing an optical parametric amplifier), which is coupled to a stationary tapered fiber. The resonator (driven by a strong control field at frequency ω_l and a weak probe field at frequency ω_p), with optical resonance frequency ω_0 and intrinsic loss $\kappa_a = \omega_0/Q$ (Q is the optical quality factor), supports a mechanical breathing mode (frequency ω_m and effective mass m). A control laser and a probe laser are applied to the system via the evanescent coupling of the optical fiber and resonator, and the field amplitudes are given by

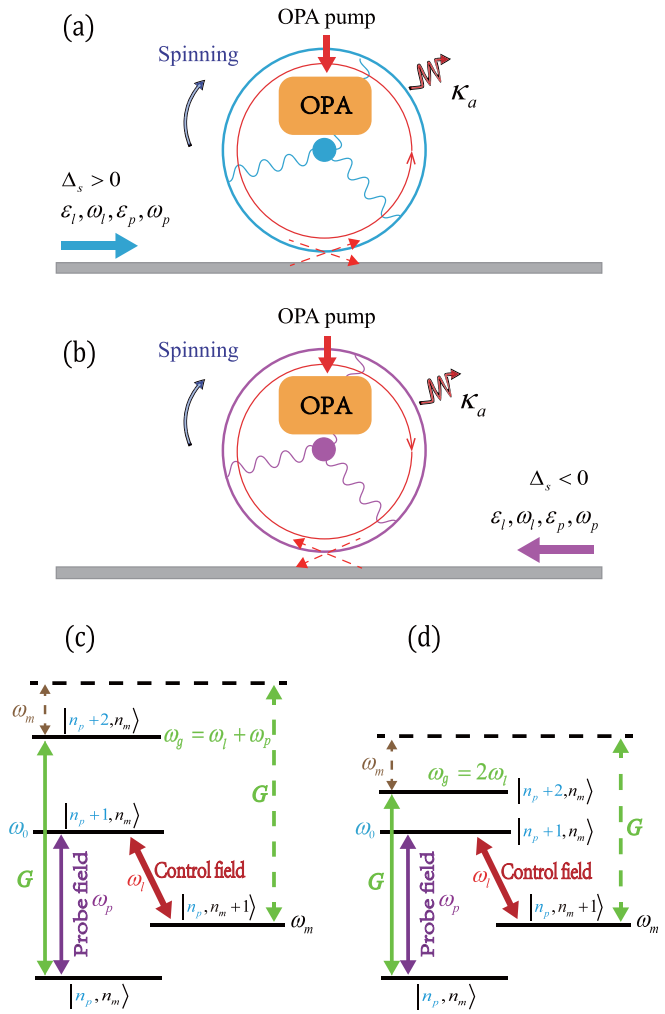

FIG. 1. Schematic diagram of the spinning optomechanical system. A rotating whispering-gallery-mode microresonator (containing an OPA [159–164] with frequency ω_g) is coupled to a stationary tapered fiber. The resonator supports a mechanical mode at frequency ω_m. We fix the clockwise rotation of the resonator, which causes the light circulating in the resonator to experience a Sagnac-Fizeau shift. The control-probe fields come from (a) the left side $\Delta_s > 0$ and (b) the right side $\Delta_s < 0$. The nonlinear crystal is pumped by an additional laser beam to produce parametric amplification. Also shown is the level schematic of the optomechanical system with an OPA, with pump frequencies (c) $\omega_g = \omega_l + \omega_p$ and (d) $\omega_g = 2\omega_l$, where $|n_p\rangle$ and $|n_m\rangle$ denote the number states of the cavity and the mechanical mode, respectively.

$\varepsilon_l = \sqrt{P_l/\hbar\omega_l}$ and $\varepsilon_p = \sqrt{P_p/\hbar\omega_p}$, where P_l and P_p are the control and probe powers, respectively. It is well known that due to the rotation, the optical mode frequency experiences Sagnac-Fizeau shift [51,165,166], which transforms as

$$\omega_0 \to \omega_0 + \Delta_s, \tag{1}$$

$$\Delta_s = \frac{nR\Omega\omega_0}{c}\left(1 - \frac{1}{n^2} - \frac{\lambda}{n}\frac{dn}{d\lambda}\right), \tag{2}$$

where $\Omega = \dot{\phi}$ is the angular velocity of the spinning resonator; n and R are the refractive index and radius of the resonator, respectively; and c and λ are the speed of light and the light wavelength in a vacuum, respectively. The dispersion term $dn/d\lambda$ represents a negligibly small relativistic (dispersion) correction in the Sagnac-Fizeau shift [51,61]. In Eq. (2), the first term in the parenthesis shows the Sagnac contribution which arises from the rotation of the resonators, while the two last terms with negative signs take into account the Fizeau drag due to the light propagation through a moving resonator medium. As shown in Refs. [73,167,168], the operating mechanism of the OPA is standard two-photon squeezing. Embedding the OPA in an optomechanical cavity makes the squeezed state transfer between a photon of a cavity field and a phonon of mechanical mode, which can amplify nonlinear optical responses of the system and reduce mechanical thermal noise and photon shot noise. The Hamiltonian formulation of the system reads

$$\hat{H} = \hat{H}_{\rm mech} + \hat{H}_{\rm opt} + \hat{H}_{\rm OPA} + \hat{H}_{\rm drive}, \tag{3}$$

with

$$\begin{aligned}
\hat{H}_{\rm mech} &= \frac{\hat{p}^2}{2m} + \frac{1}{2}m\omega_m^2\hat{x}^2 + \frac{\hat{p}_\phi^2}{2m(R+\hat{x})^2},\\
\hat{H}_{\rm opt} &= \hbar(\omega_0 + \Delta_s)\hat{a}^\dagger\hat{a} - \hbar\xi\hat{a}^\dagger\hat{a}\hat{x},\\
\hat{H}_{\rm OPA} &= i\hbar G(\hat{a}^{\dagger 2}e^{i\theta}e^{-i\omega_g t} - \text{H.c.}),\\
\hat{H}_{\rm drive} &= i\hbar\sqrt{\kappa_{\rm ex}}(\varepsilon_l\hat{a}^\dagger e^{-i\omega_l t} + \varepsilon_p\hat{a}^\dagger e^{-i\omega_p t} - \text{H.c.}),
\end{aligned} \tag{4}$$

where $\hat{p}$, $\hat{x}$, $\hat{\phi}$, and $\hat{p}_\phi$ denote the momentum, position, rotation angle, and angular momentum operators, respectively, with commutation relations $[\hat{x}, \hat{p}] = [\hat{\phi}, \hat{p}_\phi] = i\hbar$ [169]; H.c. stands for the Hermitian conjugate; $\hat{a}$ ($\hat{a}^\dagger$) is the annihilation (creation) operator of the cavity field with resonance frequency ω_0; $\xi = \omega_0/R$ is the optomechanical coupling; $\hat{H}_{\rm OPA}$ describes the coupling of the intracavity field with the OPA (pump frequency ω_g); G is the nonlinear gain of the OPA, which is proportional to the pump power driving amplitude; and θ is the phase of the field driving the OPA [170]. We assume that this OPA with a second-order nonlinearity crystal is excited by a pump driving with the frequency $\omega_g = \omega_l + \omega_p$ [96] in Fig. 1(c), so the signal light and idler light in the OPA have the same frequency $(\omega_l + \omega_p)/2$ [161–163,171]. In addition, $\hat{H}_{\rm drive}$ denotes the interaction of the cavity field with the control field and that of the cavity field with the probe field, with $\kappa_{\rm ex}$ the loss caused by the resonator-fiber coupling.

In the rotating frame at the control frequency ω_l, the Hamiltonian (3) becomes

$$\begin{aligned}
\hat{H}_{\rm eff} &= \hbar(\Delta_0 - \xi\hat{x} + \Delta_s)\hat{a}^\dagger\hat{a} + \frac{\hat{p}^2}{2m} + \frac{1}{2}m\omega_m^2\hat{x}^2\\
&\quad + \frac{\hat{p}_\phi^2}{2m(R+\hat{x})^2} + i\hbar G(\hat{a}^{\dagger 2}e^{-i\Delta_p t}e^{i\theta} - \text{H.c.})\\
&\quad + i\hbar\sqrt{\kappa_{\rm ex}}[(\varepsilon_l + \varepsilon_p e^{-i\Delta_p t})\hat{a}^\dagger - \text{H.c.}],
\end{aligned} \tag{5}$$

where $\Delta_0 = \omega_0 - \omega_l$ and $\Delta_p = \omega_p - \omega_l$. When the control field is injected at the red-detuned sideband of the cavity resonance ($\Delta_p = \omega_m$), the transition $|n_p, n_m + 1\rangle \leftrightarrow |n_p + 1, n_m\rangle$ occurs. Moreover, $|n_p, n_m\rangle$ couples with $|n_p + 1, n_m\rangle$ through the probe field, which is in resonance with the cavity mode ($\omega_p = \omega_0$). In this case, the destructive interference of these two excitation pathways occurs, which leads to OMIT [22]

in Fig. 1(c) with pump frequency $\omega_g = \omega_l + \omega_p$ (discussed in Secs. II–IV and VI) and Fig. 1(d) with pump frequency $\omega_g = 2\omega_l$ (Sec. V), where the OPA has almost no influence on the interference paths. With the operator expectation values defined by $a \equiv \langle \hat{a} \rangle$, $x \equiv \langle \hat{x} \rangle$, $\phi \equiv \langle \hat{\phi} \rangle$, and $p_\phi \equiv \langle \hat{p}_\phi \rangle$, the Heisenberg-Langevin equations of the spinning optomechanical system can be derived as

$$\dot{a} = -[\kappa + i(\Delta_0 - \xi x + \Delta_s)]a + \sqrt{\kappa_{\rm ex}}(\varepsilon_l + \varepsilon_p e^{-i\Delta_p t}) + 2Ga^* e^{i\theta} e^{-i\Delta_p t}, \tag{6}$$

$$m\left(\ddot{x} + \Gamma_m \dot{x} + \omega_m^2 x\right) = \hbar \xi a^* a + \frac{p_\phi^2}{mR^3}, \tag{7}$$

$$\dot{\phi} = \frac{p_\phi}{mR^2}, \tag{8}$$

$$\dot{p}_\phi = 0, \tag{9}$$

where $\kappa = (\kappa_a + \kappa_{\rm ex})/2$ and Γ_m are the dissipations of the cavity and the damping of the mechanical mode, respectively. The derivation of Eqs. (6)–(9) can be found in the Appendix. Focusing on the mean response of the system to the probe field, we write the operators for their expectation values by means of the mean-field approximation and safely ignore the quantum noise terms with strong driving conditions.

In this case, we assume the control field is much stronger than the probe field ($\varepsilon_l \gg \varepsilon_p$), which means we can use the perturbation method to deal with Eqs. (6)–(9). The control field provides a steady-state solution of the system, while the probe field is treated as the perturbation of the steady state. We then follow the standard procedure, which decomposes the expectation value of all operators as a sum of their steady-state value and small fluctuations around the steady-state value [22,43]

$$\begin{aligned} a &= a_s + A_1^+ e^{-i\Delta_p t} + A_1^- e^{i\Delta_p t} + A_2^+ e^{-2i\Delta_p t} + A_2^- e^{2i\Delta_p t}, \\ x &= x_s + X_1^+ e^{-i\Delta_p t} + X_1^- e^{i\Delta_p t} + X_2^+ e^{-2i\Delta_p t} + X_2^- e^{2i\Delta_p t}, \end{aligned} \tag{10}$$

in which A_2^+ (A_2^-) is the amplitude of second-order upper (lower) sideband and corresponds to the responses at the original frequencies $2\omega_p - \omega_l$ ($3\omega_l - 2\omega_p$). We are committed to the fundamental OMIT and its second-order sideband process, so the higher-order sidebands in Eq. (10) are ignored. By substituting Eq. (10) into Eqs. (6)–(9) and comparing the coefficients of the same order, the steady-state solutions are obtained as

$$\begin{aligned} a_s &= \frac{\sqrt{\kappa_{\rm ex}}\varepsilon_l}{\kappa + i\Delta}, \\ x_s &= \frac{\hbar \xi |a_s|^2}{m\omega_m^2} + R\left(\frac{\Omega}{\omega_m}\right)^2, \end{aligned} \tag{11}$$

where $\Delta = \Delta_0 - \xi x_s + \Delta_s$ and $\Omega = d\phi/dt$ is the angular velocity of the spinning resonator. It is clear that the revolving speed of the resonator and Sagnac-Fizeau shift Δ_s affect the values of both the mechanical displacement x_s and intracavity photon number $|a_s|^2$. Substituting Eq. (10) into Eqs. (6)–(9), we gain six algebraic equations, which can be divided into two groups. The first group describes the linear response of the probe field

$$\begin{aligned} \sigma_1(\Delta_p)A_1^+ &= i\xi a_s X_1^+ + 2Ge^{i\theta}a_s^* + \sqrt{\kappa_{\rm ex}}\varepsilon_p, \\ \sigma_2(\Delta_p)A_1^{-*} &= -i\xi a_s^* X_1^+, \\ \chi(\Delta_p)X_1^+ &= \hbar\xi(a_s A_1^{-*} + a_s^* A_1^+), \end{aligned} \tag{12}$$

while the second group corresponds to the second-order sideband process

$$\begin{aligned} \sigma_1(2\Delta_p)A_2^+ &= i\xi(a_s X_2^+ + A_1^+ X_1^+) + 2Ge^{i\theta}A_1^{-*}, \\ \sigma_2(2\Delta_p)A_2^{-*} &= -i\xi(a_s^* X_2^+ + A_1^{-*} X_1^+), \\ \chi(2\Delta_p)X_2^+ &= \hbar\xi(a_s^* A_2^+ + a_s A_2^{-*} + A_1^{-*} A_1^+), \end{aligned} \tag{13}$$

with

$$\begin{aligned} \sigma_1(n\Delta_p) &= \kappa + i\Delta - in\Delta_p, \\ \sigma_2(n\Delta_p) &= \kappa - i\Delta - in\Delta_p, \\ \chi(n\Delta_p) &= m\left(\omega_m^2 - i\Gamma_m n\Delta_p - \Delta_p^2\right). \end{aligned}$$

Moreover, we can easily get the linear and second-order nonlinear responses of the system

$$\begin{aligned} A_1^+ &= \frac{D + \sigma_2(\Delta_p)\chi(\Delta_p)}{f_3(\Delta_p)}(\sqrt{\kappa_{\rm ex}}\varepsilon_p + 2Ge^{i\theta}a_s^*), \\ X_1^+ &= \frac{\hbar\xi a_s^* \sigma_2(\Delta_p)}{D + \sigma_2(\Delta_p)\chi(\Delta_p)}A_1^+, \\ A_1^{-*} &= \frac{-i\xi a_s^*}{\sigma_2(\Delta_p)}X_1^+ \end{aligned} \tag{14}$$

and

$$\begin{aligned} A_2^+ &= \frac{-D\xi^2 a_s X_1^{+2} + i\xi f_1 A_1^+ X_1^+ - 2i\xi G e^{i\theta} a_s^* f_2 X_1^+}{\sigma_2(\Delta_p) f_3(2\Delta_p)}, \\ X_2^+ &= \frac{\hbar\xi[\sigma_2(2\Delta_p)a_s^* A_2^+ + \sigma_2(2\Delta_p)A_1^+ A_1^{-*} - i\xi a_s A_1^{-*} X_1^+]}{f_2}, \\ A_2^- &= \frac{i\xi}{\sigma_2(2\Delta_p)^*}(a_s X_2^- + A_1^- X_1^-), \end{aligned} \tag{15}$$

where

$$\begin{aligned} D &= i\hbar\xi^2|a_s|^2, \\ f_1 &= iD\Delta_p + \sigma_2(\Delta_p)\sigma_2(2\Delta_p)\chi(2\Delta_p), \\ f_2 &= D + \sigma_2(2\Delta_p)\chi(2\Delta_p), \\ f_3(n\Delta_p) &= 2iD\Delta + \sigma_1(n\Delta_p)\sigma_2(n\Delta_p)\chi(n\Delta_p). \end{aligned}$$

By using the standard input-output relations, i.e.,

$$a_{\rm out}(t) = a_{\rm in}(t) - \sqrt{\kappa_{\rm ex}}a(t), \tag{16}$$

we obtain the expectation value of the output field of this system

$$\begin{aligned} a_{\rm out}(t) = C_1 e^{-i\omega_l t} + C_2 e^{-i\omega_p t} &- \sqrt{\kappa_{\rm ex}}A_1^- e^{-i(2\omega_l - \omega_p)t} \\ &- \sqrt{\kappa_{\rm ex}}A_2^+ e^{-i(2\omega_p - \omega_l)t} - \sqrt{\kappa_{\rm ex}}A_2^- e^{-i(3\omega_l - 2\omega_p)t}, \end{aligned} \tag{17}$$

where $C_1 = \varepsilon_l - \sqrt{\kappa_{\rm ex}}a_s$ and $C_2 = \varepsilon_p - \sqrt{\kappa_{\rm ex}}A_1^+$. The first term of Eq. (17) denotes the output with control frequency ω_l, while the second and third terms represent the anti-Stokes and Stokes fields, respectively. The terms $-\sqrt{\kappa_{\rm ex}}A_2^+ e^{-i(2\omega_p - \omega_l)t}$

and $-\sqrt{\kappa_{\rm ex}}A_2^- e^{-i(3\omega_l-2\omega_p)t}$ are concerned with the second-order upper and lower sidebands, respectively [43].

We now introduce the dimensionless quantity to define the efficiency of the second-order upper and lower sidebands [43,172]

$$\eta_1 = \left|-\frac{\sqrt{\kappa_{\rm ex}}A_2^+}{\varepsilon_p}\right|, \tag{18}$$

$$\eta_2 = \left|-\frac{\sqrt{\kappa_{\rm ex}}A_2^-}{\varepsilon_p}\right|, \tag{19}$$

where the amplitude of the probe pulse is treated as a basic scale to gauge the amplitudes of the output sidebands η_1 and η_2. The associated group delay of the second-order upper sideband turns out to be [23,173,174]

$$\tau_1 = \left.\frac{d\arg\left(-\frac{\sqrt{\kappa_{\rm ex}}A_2^+}{\varepsilon_p}\right)}{2d\Delta_p}\right|_{\Delta_p=\omega_m}. \tag{20}$$

A positive group delay ($\tau_1 > 0$) corresponds to the slow light phenomenon, while a negative group delay ($\tau_1 < 0$) corresponds to the fast light phenomenon [23,175].

III. RESULTS AND DISCUSSION

In our numerical simulations, to demonstrate that the observation of the second-order sidebands in a resonator assisted by an OPA is within current experimental reach, we calculate Eqs. (18)–(20) with parameters from Refs. [51,176,177]: $\lambda = 1550$ nm, $R = 0.25$ mm (the resonator radius), $m = 25$ ng, $n = 1.44$, $Q = \omega_0/\kappa = 4.5 \times 10^7$, $\omega_m = 100$ MHz, $\Gamma_m = 0.1$ MHz, $\kappa_a = \kappa_{\rm ex} = \omega_0/Q$, $P_p = 0.05P_l$, and $\Delta_0 = \omega_m$. We rotate the resonator clockwise, where $\Omega > 0$ stands for the light coming from the left-hand side and $\Omega < 0$ denotes the light coming from the right-hand side.

To see the influence of resonator rotation and the OPA on the second-order sideband generation, the efficiency of second-order upper sideband generation is investigated as a function of frequency Δ_p/ω_m shown in Fig. 2. In Fig. 2(a) we show that the efficiency η_1 of the second-order upper sideband varies with Δ_p without the participation of the OPA, i.e., the nonlinear gain of the OPA $G = 0$ and the phase of the field driving the OPA $\theta = 0$. For a stationary resonator, we find two peaks of second-order sideband spectra and a local minimum near the resonance condition $\Delta_p = \omega_m$. By spinning the resonator, the peak position of η_1 has different moves when the driving fields come from different directions. By adjusting the frequency Δ_p/ω_m, we can get enhanced efficiency of the second-order sideband while driving the resonator from one direction and suppressed efficiency while driving from the opposite direction. For example, within Δ_p/ω_m in the range from 0.99 to 1, η_1 is enhanced in the case of $\Omega > 0$, while it is suppressed in the case of $\Omega < 0$. Obviously, this spinning-induced direction-dependent nonreciprocal behavior can be attributed to the optical Sagnac effect induced by a spinning resonator. As shown in Fig. 2(b), the efficiency η_1 gets larger in the presence of the OPA. To be more specific, for $G = 0.2\kappa$, $\theta = 0$, and $\Omega = 20$ kHz, the efficiency η_1 can increase from 19.5% to 27.2% at $\Delta_p = 0.997\omega_m$. When the system is driven from the right, i.e., $\Omega = -20$ kHz, the efficiency η_1 also can

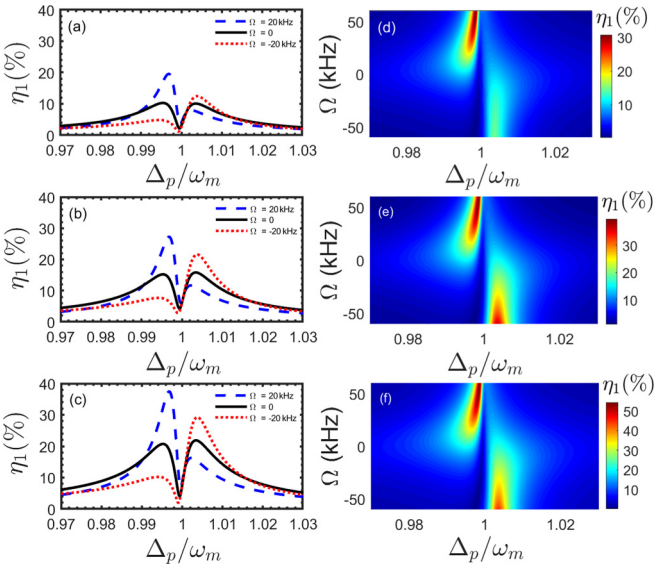

FIG. 2. Efficiency η_1 of the second-order upper sideband generation as a function of Δ_p for different values of Ω and incident directions of light, where the nonlinear gain and phase of the probe field of the OPA are fixed at (a) $G = 0$ and $\theta = 0$, (b) $G = 0.2\kappa$ and $\theta = 0$, and (c) $G = 0.2\kappa$ and $\theta = 3\pi/2$. The η_1 varies with Δ_p and Ω for different values (d) $G = 0$ and $\theta = 0$, (e) $G = 0.2\kappa$ and $\theta = 0$, and (f) $G = 0.2\kappa$ and $\theta = 3\pi/2$. The other parameters are $P_p = 0.05P_l$, $P_l = 1$ mW, $\lambda = 1550$ nm, $R = 0.25$ mm, $m = 25$ ng, $n = 1.44$, $Q = \omega_0/\kappa = 4.5 \times 10^7$, $\omega_m = 100$ MHz, $\Gamma_m = 0.1$ MHz, $\kappa_a = \kappa_{\rm ex} = \omega_0/Q$, $P_p = 0.05P_l$, and $\Delta_0 = \omega_m$. With these parameters, we obtain the Sagnac-Fizeau shift $\Delta_s = (15.082\ \text{MHz}, 0, 15.082\ \text{MHz})$ or $\Delta_s/\omega_m = (0.1508, 0, -0.1508)$, which corresponds to the angular velocity $\Omega = (20\ \text{kHz}, 0, -20\ \text{kHz})$ of the cavity.

increase from 12.4% to 21.6% at $\Delta_p = 1.004\omega_m$. Figure 2(c) shows that the efficiency η_1 can also be adjusted by tuning θ. As can be seen clearly when θ changes from $\theta = 0$ to $\theta = 3\pi/2$, in the case of $G = 0.2\kappa$ and $\Omega = 20$ kHz, the maximum value of η_1 increases to 37.4%. In the case of $\Omega = -20$ kHz, the maximum value increases to 29.2%. We see that the efficiency of the second-order upper sideband is sensitive to the variation of the nonlinear gain of the OPA and phase of the field driving the OPA, which indicates the advantage of using a hybrid nonlinear system. According to Eqs. (14) and (15), such phenomena coming from the amplitudes of second-order sidebands A_2^+ and A_2^- are directly related to the Sagnac-Fizeau shift and the OPA. To show the influence of the OPA on the second-order sideband generation more clearly, the efficiency η_1 is shown as a function of both Δ_p and Ω in Figs. 2(d)–2(f).

To explore the role of the OPA in this resonator, we illustrate in Fig. 3 the efficiency η_1 of the second-order upper sideband versus the probe-pulsed detuning Δ_p with different nonlinear gain G of the OPA and phase θ of the field driving the OPA, when the system is driven from the right-hand side ($\Omega = -20$ kHz). We find in Fig. 3(a) that when the nonlinear gain G of the OPA increases from 0 to $G = 0.6\kappa$, the efficiency η_1 can be significantly enhanced. The enhancement effect at the probe-pulsed detuning $\Delta_p/\omega_m < 1$ is much weaker than at $\Delta_p/\omega_m > 1$. Figure 3(c) shows that

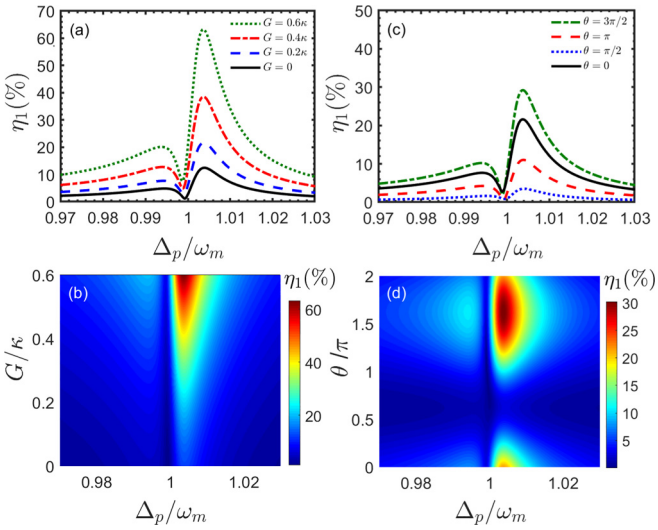

FIG. 3. Efficiency η_1 of the second-order upper sideband generation as a function of the probe-pulsed detuning Δ_p for different (a) nonlinear gain G of the OPA with $\theta = 0$ and (c) phase θ with $G = 0.2\kappa$. (b) Variation of η_1 with Δ_p and G for $\theta = 0$. (d) Variation of η_1 with Δ_p and θ for $G = 0.2\kappa$. The angular velocity of the spinning resonator is fixed at $\Omega = -20$ kHz. The other parameters are the same as in Fig. 2.

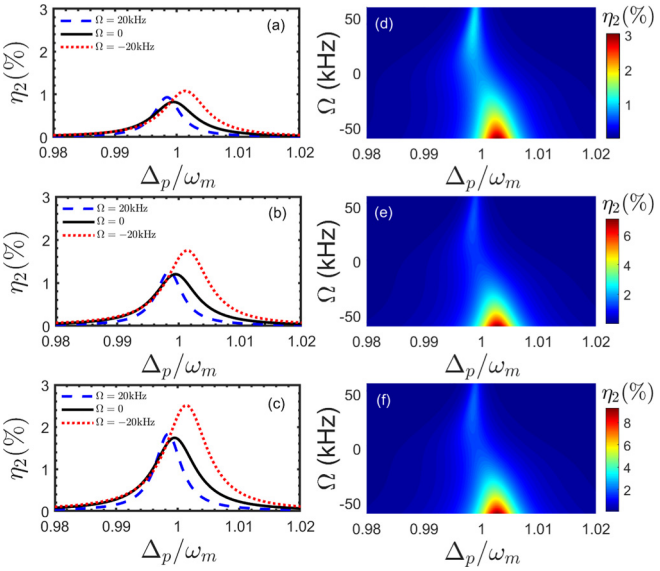

FIG. 4. Efficiency η_2 of the second-order lower sideband generation as a function of Δ_p for different values of Ω and incident directions of light, where the nonlinear gain and phase of the probe field of the OPA are fixed at (a) $G = 0$ and $\theta = 0$, (b) $G = 0.2\kappa$ and $\theta = 0$, and (c) $G = 0.2\kappa$ and $\theta = 3\pi/2$. The η_2 varies with Δ_p and Ω for different values (d) $G = 0$ and $\theta = 0$, (e) $G = 0.2\kappa$ and $\theta = 0$, and (f) $G = 0.2\kappa$ and $\theta = 3\pi/2$. The other parameters are the same as in Fig. 2.

the second-order sideband behavior of the output field can also be adjusted by tuning θ. In the case of $G = 0.2\kappa$, we find that compared with $\theta = 0$, both $\theta = \pi/2$ and $\theta = \pi$ result in lower efficiency η_1 of the second-order upper sideband, but $\theta = 3\pi/2$ leads to enhanced efficiency. Figure 3(d) plots η_1 as a function of detuning Δ_p and the phase θ of the OPA. In the range shown, the maximum value of efficiency η_1 is about 30.2% at $\theta = 1.6\pi$ and $\Delta_p = 1.004\omega_m$. Specifically, the efficiency is enhanced when $\theta \in (1.6\pi, 2\pi)$ and suppressed at other values. In addition, as is illustrated in Figs. 3(b) and 3(d), regardless of whether the nonlinear gain G and θ increases, the maxima of the efficiency η_1 are still located at the same position of the probe-pulsed detuning. This phenomenon can be explained by Refs. [22,43], which show there are some connections between OMIT and the second-order sideband process. When OMIT occurs, the second-order sideband process is subdued. The linewidth of the OMIT window is related to the intracavity photon number

$$\Gamma_{\mathrm{OMIT}} \approx \Gamma_{\mathrm{m}} + \frac{\xi^2 x_{\mathrm{ZPF}}^2}{\kappa}|a_s|^2, \tag{21}$$

where $x_{\mathrm{ZPF}} = \sqrt{\hbar/2m\omega_{\mathrm{m}}}$. By perturbation theory, we can get the intracavity photon number $|a_s|^2$ in Eq. (11), which is independent of other perturbation terms such as the probe pulse and nonlinear gain of the OPA. In other words, the positions of these local maxima of the sideband spectra only depend on the intrinsic structural parameters of an optomechanical system and the intensity of the control field. As a result, the OPA not only improves the sideband efficiency of the second-order sideband but also keeps the locality of maximum values of the sideband efficiency.

In Fig. 4 we show the influence of resonator rotation and the OPA on the second-order lower sideband generation. As shown in Fig. 4(a), unlike the second-order upper sideband, the second-order lower sideband has no local minimum but only one peak. The efficiency is much smaller than the second-order upper sideband. Specifically, with neither resonator rotation nor the OPA drive ($G = 0$ and $\Omega = 0$), both peaks of η_1 are about 19.6% and the peak of η_2 is only 0.82%. Furthermore, the second-order lower sideband exhibits nonreciprocal characteristics due to the rotation of the resonator, which is more pronounced at $\Delta_p/\omega_m > 1$. Specifically, compared with the stationary resonator (i.e., no spinning with $\Omega = 0$), the spinning resonator increases for $\Omega = -20$ kHz, while it decreases for $\Omega = 20$ kHz at $\Delta_p/\omega_m > 1$ in Fig. 4(a). In Fig. 4(d) we find that for the same resonator speed, the enhancement effect is more pronounced when the device is driven from the right side ($\Omega < 0$) than from the left side ($\Omega > 0$). For example, for $\Omega = -60$ kHz, the maximum value of η_2 is 3.04% at $\Delta_p/\omega_m = 1.003$. For $\Omega = 60$ kHz, the maximum value of η_2 is 0.97% at $\Delta_p/\omega_m = 0.999$. In Figs. 4(b) and 4(c), as with the second-order upper sideband, the presence of the OPA significantly improves the efficiency of the second-order lower sideband, which also keeps the locality of maximum values of the sideband efficiency. Specifically, for $\Omega = -20$ kHz, when the nonlinear gain G of the OPA increases from 0 to 0.2κ, the maximum value of η_2 increases from 1.08% to 1.75% at $\Delta_p/\omega_m = 1.001$. In addition, when the phase θ of the OPA increases from 0 to $3\pi/2$, the maximum value of η_2 can be increased to 2.51%, which is more than twice the value without the OPA.

We show that the presence of the OPA only causes a change in the peak of η_1 and has almost no influence on asymmetry [see black solid line in Figs. 2(a)–2(c) for $\Omega = 0$

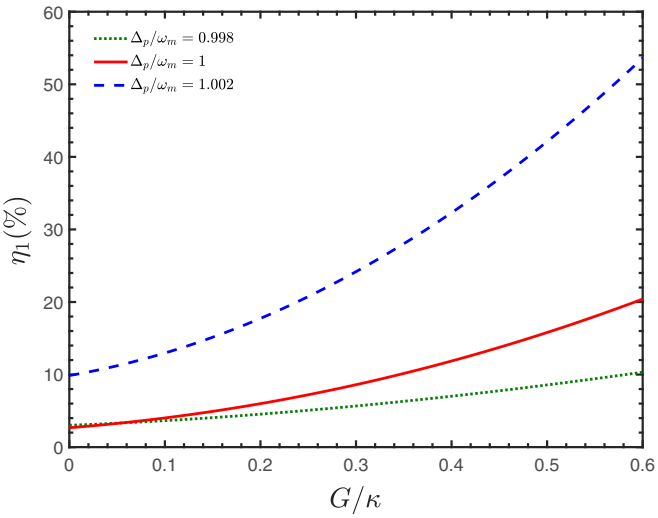

FIG. 5. Efficiency η_1 of the second-order upper sideband generation as a function of the nonlinear gain G of the OPA for different probe-pulsed detuning Δ_p, where $\theta = 0$ and $\Omega = 0$. The other parameters are the same as in Fig. 2.

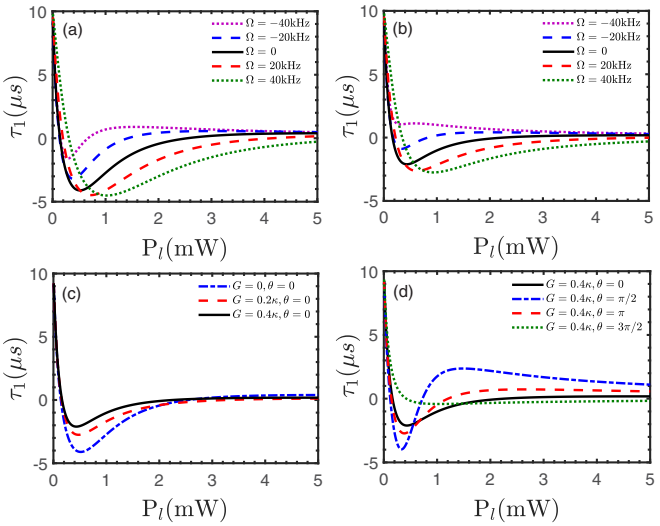

FIG. 6. Optical group delay of the second-order upper sideband τ_1 plotted as a function of P_l with different values of Ω and incident directions of light (a) without the OPA and (b) in the presence of the OPA effect at $G = 0.4\kappa$ and $\theta = 0$. The τ_1 is plotted as a function of P_l with different (c) nonlinear gain G and (d) phase θ of the field driving the OPA, where $\Omega = 0$. The other parameters are the same as in Fig. 2.

and black solid line in Figs. 4(a)–4(c) for $\Omega = 0$]. Without the OPA ($G = 0$), the asymmetric line shape of η_1 with regard to $\Delta_p = \omega_m$ and the η_2 peak being not exactly at $\Delta_p = \omega_m$ come from the spinning of the resonator. In this case, the mean mechanical displacement x_s in Eq. (11) is made up of two terms. The first term is proportional to the intracavity photon number $|a_s|^2$, which is closely related to the Sagnac-Fizeau shift $\Delta_s = \frac{nR\Omega\omega_0}{c}(1 - \frac{1}{n^2} - \frac{\lambda}{n}\frac{dn}{d\lambda})$ in Eq. (2) or, equivalently, very sensitive to the angular velocity Ω of the resonator and incident direction of input fields, thus giving rise to the nonreciprocal behavior. The second term $R(\Omega/\omega_m)^2$ of x_s makes the mechanical displacement larger due to the rotation. The existence of these two terms together affects the second-order upper and lower sidebands in Eqs. (18) and (19), which lead to the asymmetry of η_1 with regard to $\Delta_p = \omega_m$ and the η_2 peak being not exactly at $\Delta_p = \omega_m$, as shown in Figs. 2–4.

In this case, $R(\Omega/\omega_m)^2$ of x_s in Eq. (11) originates from an extra term in the Hamiltonian of our model due to the rotation, i.e., the rotational kinetic energy term $\hat{p}_\phi^2/2m(R+\hat{x})^2$ in Eq. (4), which is different from the usual situation in Ref. [43]. Since $x/R \ll 1$ ($x = \langle\hat{x}\rangle$ denotes the expectation value of $\hat{x}$), the term $\hat{p}_\phi^2/2m(R+\hat{x})^2$ is approximately equal to $-\hat{p}_\phi^2\hat{x}/mR^3 + \hat{p}_\phi^2/2mR^2$ (neglecting second- and higher-order small quantities about x/R). This means that there is an extra force $-\hat{p}_\phi^2\hat{x}/mR^3$ exerted on the mechanical mode making it deviate from its original equilibrium position.

To clearly see the influence of the nonlinear gain G of the OPA on the second-order sideband generation, the efficiency η_1 is investigated as a function of the nonlinear gain G for different probe-pulsed detuning Δ_p, as shown in Fig. 5. In detail, when G increases from 0 to 0.6κ in the case of $\Delta_p/\omega_m = 1.002$, the system provides an enhancement of more than five times for the sideband efficiency η_1. In general, with the nonlinear gain G increasing, the efficiency η_1 of the second-order upper sideband generation increases obviously. The reason is that when the OPA is pumped at $\omega_g = \omega_l + \omega_p$, i.e., twice the frequency of the anti-Stokes field, the parametric frequency conversion between this anti-Stokes field and phonon mode can provide another way to generate an optical second-order sideband, leading to the enhancement of a second-order sideband.

IV. TUNABLE SLOW AND FAST LIGHT

We know the slow light effect is an important result of OMIT, which can be described by the optical group delay [23,101–104]. It is similar to that of electromagnetically induced transparency; in the region of the narrow transparency window, the rapid phase dispersion can cause the group delay given by Eq. (20). A positive group delay ($\tau_1 > 0$) corresponds to slow light propagation and a negative group delay ($\tau_1 < 0$) indicates fast light propagation.

In previous work [23,175], it has been demonstrated that the delay of the transmitted light is only relevant to the pump power in a conventional optomechanical system. In our model, we see clearly from Fig. 6 that the delay time of the second-order upper sideband can be adjusted not only by tuning the speed and direction of rotation of the resonator but also by adjusting the nonlinear gain of the OPA and phase of the field driving the OPA. In Figs. 6(a) and 6(b) we investigate the group delay of the second-order upper sideband τ_1 as a function of control laser power P_l for different Ω. We find that when the resonator is stationary ($\Omega = 0$), with the power increasing, τ_1 tends to advance and even switches into fast light. However, in the presence of resonator rotation, the delay time of the second-order upper sideband will be prolonged at high control powers, which is useful for storage. In detail, as shown in Fig. 6(a), for a resonator speed of 20 kHz, the group delay time τ_1 increases when the resonator is driven from the right side ($\Omega = -20$ kHz) and decreases when the resonator

is driven from the left side ($\Omega = 20$ kHz). The group delay can still reach the conversion from fast light to slow light at this point. Increasing the resonator speed to 40 kHz, at high control power, when the resonator is driven from the right side ($\Omega = -40$ kHz), the group delay of the second-order sideband is always positive, i.e., slow light is obtained. When the resonator is driven from the left side ($\Omega = 40$ kHz), the group delay is always negative and fast light can be obtained. At this point, the switching between fast and slow light disappears. In Fig. 6(b) we show the results of group delay τ_1 versus control laser power P_l in the presence of the OPA. In the low-power range, the addition of the OPA increases the value of τ_1. More interestingly, at $\Omega = -40$ kHz, the fast and slow light conversion behavior of the group delay disappears, where only a slow light effect is obtained.

Now we discuss the influence of the presence of the OPA on the delay time of the second-order sideband. In Figs. 6(c) and 6(d) we display the group delay τ_1 as a function of the control power P_l for different parameters of nonlinear gain G and phase θ of the field driving the OPA, where the resonator is stationary. When the OPA is considered in the optomechanical system, as is expected, the delay time of the second-order upper sideband generation obviously increases with the increasing power. With the nonlinear gain G increasing from 0 to 0.4κ, the group delay τ_1 accordingly increases, while the trend of switching between fast and slow light effects remains unchanged. In Fig. 6(d) we see that the τ_1 is sensitive to the variation of the phase of the OPA. When $\theta = \pi/2$, τ_1 exhibits a significant transition from fast to slow light; in other words, the delay time significantly decreases at low power and increases at high power. Interestingly, for $\theta = 3\pi/2$, the valley of the τ_1 disappears in the low-power range, whereas the group delay exhibits a fast light effect ($\tau_1 < 0$) in the high-power range. Physically, from Eq. (15), when the OPA is added inside the optomechanically coupled system, the quantum interference effect between the probe field and second-order sideband process is directly related to the phase of the OPA, so the optical-response properties for the probe field become phase sensitive.

As shown in Fig. 7, the group delay τ_1 varies with the rotation speed of the resonator $|\Omega|$ at a fixed control power, where the red sideband $\Delta_p = \omega_m$ is also presented. We find that the group delay can achieve the transition from fast to slow light regardless of the direction of incidence of the input fields but with very significant differences. If $\Omega > 0$ (the driving fields come from the left-hand side of the fiber), when the rotation speed reaches 101 kHz, the group delay τ_1 experiences the conversion from $\tau_1 < 0$ to $\tau_1 > 0$. However, if $\Omega < 0$ (driving from the right-hand side of the fiber), when the rotation speed reaches 30 kHz, τ_1 experiences the conversion from $\tau_1 < 0$ to $\tau_1 > 0$. Therefore, we realize the conversion between the fast light and slow light by controlling the incident direction of the input fields in the spinning system. In the above discussion, we see that the group delay of the second-order upper sideband is sensitive to the variation of the rotation speed of the resonator, the direction of incidence of the input fields, and the phase of the field driving the OPA. In Fig. 8(a) the group delay τ_1 of the second-order upper sideband is plotted as a function of control power P_l and the rotation speed of the resonator Ω. In Fig. 8(b) τ_1 is plotted as a function of control power P_l

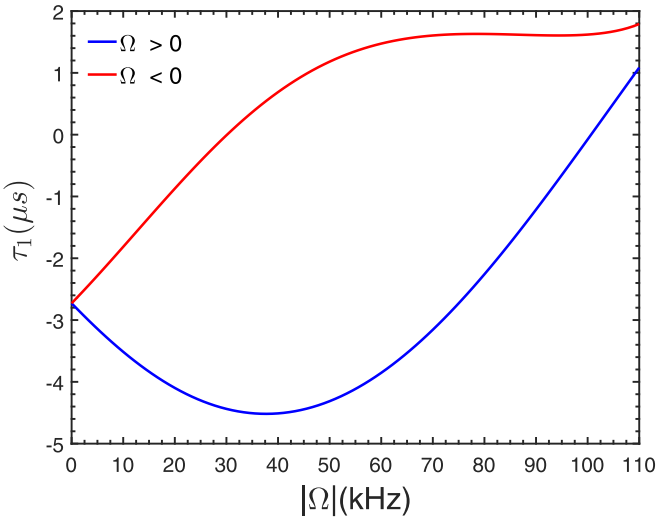

FIG. 7. Group delay of the second-order upper sideband τ_1 varying with the spinning angular velocity $|\Omega|$ at $\Omega > 0$ and $\Omega < 0$, with $G = 0.4\kappa$ and $\theta = 0$. The power of the control field P_l is 1 mW. The other parameters are the same as in Fig. 6.

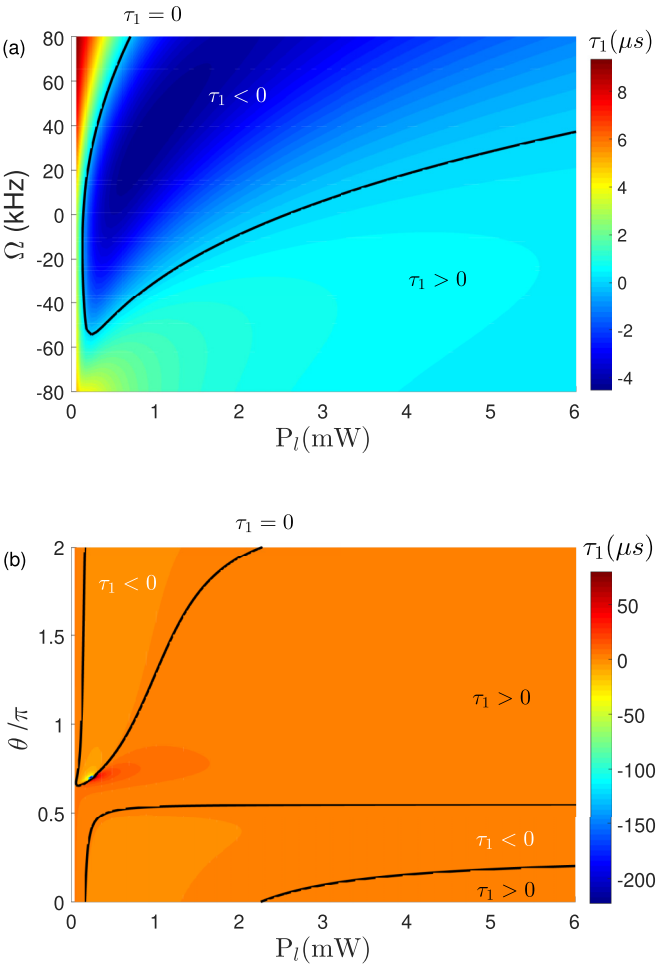

FIG. 8. Group delay of the second-order upper sideband τ_1 varying with (a) P_l and Ω at $G = 0$ and $\theta = 0$ and (b) P_l and θ at $G = 0.4\kappa$ and $\Omega = 0$. The black curves correspond to $\tau_1 = 0$. The other parameters are the same as in Fig. 6.

and the phase θ of the field driving the OPA. The black curves correspond to $\tau_1 = 0$. In this case, we can obtain the slow light effect or fast light effect by properly selecting the values of P_l, Ω, and θ. Moreover, a tunable switch from fast to slow light can be realized by adjusting their values.

V. INFLUENCE OF CHANGING THE DRIVING FREQUENCY OF THE OPA ON THE EFFICIENCY

The optical degenerate parametric amplifier, a second-order optical crystal in nature, can generate pairs of down-converted photons and show nearly perfect single or dual squeezing [159–164]. As is well known, placing an OPA pumped by an external laser in the optomechanical cavity can modulate the optomechanical coupling, which can lead directly to optical amplification [68]. We can discuss the influence of different pump frequencies of the driving OPA on the sidebands and compare the amplification of the second-order sidebands in both cases. Now we vary the frequency of the laser field driving the OPA, so the OPA is excited by a pump drive with the frequency $\omega_g = 2\omega_l$ [160], as shown in Fig. 1(d). The pump photon with frequency $\omega_g = 2\omega_l$ is down-converted into an identical pair of photons with frequency ω_l after passing through the second-order nonlinearity crystal. The $\hat{H}_{\rm OPA}$ reads

$$\hat{H}_{\rm OPA} = i\hbar G(\hat{a}^{\dagger 2}e^{i\theta}e^{-2i\omega_l t} - \text{H.c.}). \tag{22}$$

The total Hamiltonian of the system in the rotating frame at the laser frequency ω_l is given by

$$\begin{aligned}\hat{H}_{\rm eff} =& \hbar(\Delta_0 - \xi\hat{x} + \Delta_s)\hat{a}^\dagger\hat{a} + \frac{\hat{p}^2}{2m} + \frac{1}{2}m\omega_m^2\hat{x}^2 \\ &+ \frac{\hat{p}_\phi^2}{2m(R+\hat{x})^2} + i\hbar G(\hat{a}^{\dagger 2}e^{i\theta} - \text{H.c.}) \\ &+ i\hbar\sqrt{\kappa_{\rm ex}}[(\varepsilon_l + \varepsilon_p e^{-i\Delta_p t})\hat{a}^\dagger - \text{H.c.}].\end{aligned} \tag{23}$$

We can get the equations of motion

$$\begin{aligned}\dot{a} =& -[\kappa + i(\Delta_0 - \xi x + \Delta_s)]a \\ &+ \sqrt{\kappa_{\rm ex}}(\varepsilon_l + \varepsilon_p e^{-i\Delta_p t}) + 2Ge^{i\theta}a^*,\end{aligned} \tag{24}$$

$$m\big(\ddot{x} + \Gamma_m\dot{x} + \omega_m^2 x\big) = \hbar\xi a^* a + \frac{p_\phi^2}{mR^3}, \tag{25}$$

$$\dot{\phi} = \frac{p_\phi}{mR^2}, \tag{26}$$

$$\dot{p}_\phi = 0, \tag{27}$$

where we write the operators for their expectation values by the mean-field approximation. The steady-state solutions of the system are obtained as

$$\begin{aligned}\tilde{a}_s &= \frac{2Ge^{i\theta} + \kappa - i\tilde{\Delta}}{\kappa^2 + \tilde{\Delta}^2 - 4G^2}, \\ \tilde{x}_s &= \frac{\hbar\xi|\tilde{a}_s|^2}{m\omega_m^2} + R\left(\frac{\Omega}{\omega_m}\right)^2,\end{aligned} \tag{28}$$

where $\tilde{\Delta} = \Delta_0 - \xi\tilde{x}_s + \Delta_s$. It is worth noting that here, unlike Eq. (11), the intracavity photon number $|\tilde{a}_s|^2$ and displacement of mechanical oscillator $\tilde{x}_s$ strongly depend on the magnitude of nonlinear gain G and phase θ of the OPA. Equations (24)–(27) can be solved analytically with the linearized ansatz

$$\begin{aligned}a &= \tilde{a}_s + \tilde{A}_1^+ e^{-i\Delta_p t} + \tilde{A}_1^- e^{i\Delta_p t} + \tilde{A}_2^+ e^{-2i\Delta_p t} + \tilde{A}_2^- e^{2i\Delta_p t}, \\ x &= \tilde{x}_s + \tilde{X}_1^+ e^{-i\Delta_p t} + \tilde{X}_1^- e^{i\Delta_p t} + \tilde{X}_2^+ e^{-2i\Delta_p t} + \tilde{X}_2^- e^{2i\Delta_p t}.\end{aligned}$$

After the ansatz, we obtain six algebra equations, which can be divided into two groups

$$\begin{aligned}\tilde{\sigma}_1(\Delta_p)\tilde{A}_1^+ &= i\xi\tilde{a}_s\tilde{X}_1^+ + 2Ge^{i\theta}\tilde{A}_1^{-*} + \sqrt{\kappa_{\rm ex}}\varepsilon_p, \\ \tilde{\sigma}_2(\Delta_p)\tilde{A}_1^{-*} &= -i\xi\tilde{a}_s^*\tilde{X}_1^+ + 2Ge^{-i\theta}\tilde{A}_1^+, \\ \chi(\Delta_p)\tilde{X}_1^+ &= \hbar\xi(\tilde{a}_s\tilde{A}_1^{-*} + \tilde{a}_s^*\tilde{A}_1^+)\end{aligned} \tag{29}$$

and

$$\begin{aligned}\tilde{\sigma}_1(2\Delta_p)\tilde{A}_2^+ &= i\xi(\tilde{a}_s\tilde{X}_2^+ + \tilde{A}_1^+\tilde{X}_1^+) + 2Ge^{i\theta}\tilde{A}_2^{-*}, \\ \tilde{\sigma}_2(2\Delta_p)\tilde{A}_2^{-*} &= -i\xi(\tilde{a}_s^*\tilde{X}_2^+ + \tilde{A}_1^{-*}\tilde{X}_1^+) + 2Ge^{-i\theta}\tilde{A}_2^+, \\ \chi(2\Delta_p)\tilde{X}_2^+ &= \hbar\xi(\tilde{a}_s\tilde{A}_2^{-*} + \tilde{a}_s^*\tilde{A}_2^+ + \tilde{A}_1^+\tilde{A}_1^{-*}),\end{aligned} \tag{30}$$

with

$$\begin{aligned}\tilde{\sigma}_1(n\Delta_p) &= \kappa + i\tilde{\Delta} - in\Delta_p, \\ \tilde{\sigma}_2(n\Delta_p) &= \kappa - i\tilde{\Delta} - in\Delta_p, \\ \chi(n\Delta_p) &= m\big(\omega_m^2 - i\Gamma_m n\Delta_p - \Delta_p^2\big).\end{aligned}$$

We get the linear and second-order nonlinear responses of the system

$$\begin{aligned}\tilde{A}_1^+ &= \frac{\tilde{D} + \tilde{\sigma}_2(\Delta_p)\chi(\Delta_p)}{\tilde{f}_4(\Delta_p) + \tilde{f}_3(\Delta_p)}\sqrt{\kappa_{\rm ex}}\varepsilon_p, \\ \tilde{X}_1^+ &= \frac{\hbar\xi[2Ge^{-i\theta}\tilde{a}_s + \tilde{a}_s^*\tilde{\sigma}_2(\Delta_p)]}{\tilde{D} + \tilde{\sigma}_2(\Delta_p)\chi(\Delta_p)}\tilde{A}_1^+, \\ \tilde{A}_1^{-*} &= \frac{-i\xi\tilde{a}_s^*}{\tilde{\sigma}_2(\Delta_p)}\tilde{X}_1^+ + \frac{2Ge^{-i\theta}}{\tilde{\sigma}_2(\Delta_p)}\tilde{A}_1^+\end{aligned} \tag{31}$$

and

$$\begin{aligned}\tilde{A}_2^+ &= \frac{i\hbar\xi^2\tilde{f}_6\tilde{A}_1^+\tilde{A}_1^{-*} + \tilde{f}_7\tilde{A}_1^{-*}\tilde{X}_1^+ + i\xi\tilde{f}_2\tilde{A}_1^+\tilde{X}_1^+}{\tilde{f}_4(2\Delta_p) + \tilde{f}_3(2\Delta_p)}, \\ \tilde{X}_2^+ &= \frac{\hbar\xi[\tilde{f}_5\tilde{A}_2^+ - i\xi\tilde{a}_s\tilde{A}_1^{-*}\tilde{X}_1^+ + \tilde{\sigma}_2(2\Delta_p)\tilde{A}_1^+\tilde{A}_1^{-*}]}{\tilde{f}_2}, \\ \tilde{A}_2^- &= \frac{i\xi}{\tilde{\sigma}_2(2\Delta_p)^*}(\tilde{a}_s\tilde{X}_2^- + \tilde{A}_1^-\tilde{X}_1^-) + \frac{2Ge^{i\theta}}{\tilde{\sigma}_2(2\Delta_p)^*}\tilde{A}_2^{+*},\end{aligned} \tag{32}$$

where

$$\begin{aligned}\tilde{D} &= i\hbar\xi^2|\tilde{a}_s|^2, \\ \tilde{f}_2 &= \tilde{D} + \tilde{\sigma}_2(2\Delta_p)\chi(2\Delta_p), \\ \tilde{f}_3(n\Delta_p) &= 2i\tilde{D}\Delta + \tilde{\sigma}_1(n\Delta_p)\tilde{\sigma}_2(n\Delta_p)\chi(n\Delta_p), \\ \tilde{f}_4(n\Delta_p) &= 2i\hbar\xi^2 G\big(\tilde{a}_s^{*2}e^{i\theta} - \tilde{a}_s^2 e^{-i\theta}\big) - 4G^2\chi(n\Delta_p), \\ \tilde{f}_5 &= 2Ge^{-i\theta}\tilde{a}_s + \tilde{a}_s^*\tilde{\sigma}_2(2\Delta_p), \\ \tilde{f}_6 &= -2Ge^{i\theta}\tilde{a}_s^* + \tilde{a}_s\tilde{\sigma}_2(2\Delta_p), \\ \tilde{f}_7 &= \hbar\xi^3\tilde{a}_s^2 - 2i\xi Ge^{i\theta}\chi(2\Delta_p).\end{aligned}$$

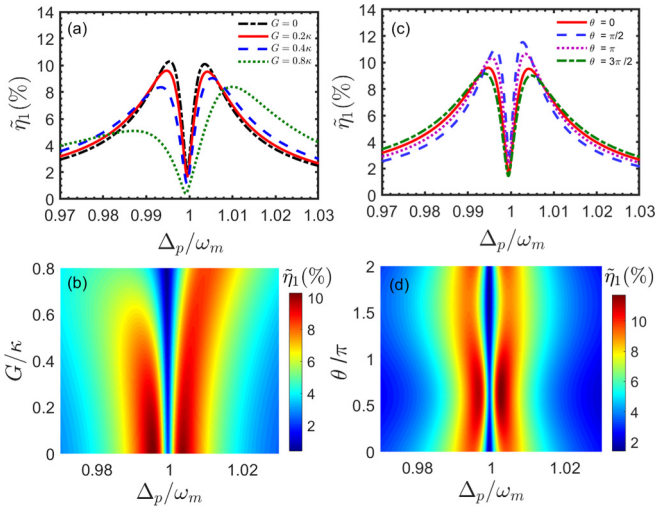

FIG. 9. Efficiency $\tilde{\eta}_1$ of the second-order upper sideband generation as a function of the probe-pulsed detuning Δ_p for different (a) nonlinear gain G for $\theta = 0$ and (c) phase θ of the field driving the OPA for $G = 0.2\kappa$. (b) Variation of $\tilde{\eta}_1$ with Δ_p and G for $\theta = 0$. (d) Variation of $\tilde{\eta}_1$ with Δ_p and θ for $G = 0.2\kappa$. The resonator is stationary ($\Omega = 0$). The other parameters are the same as in Fig. 2.

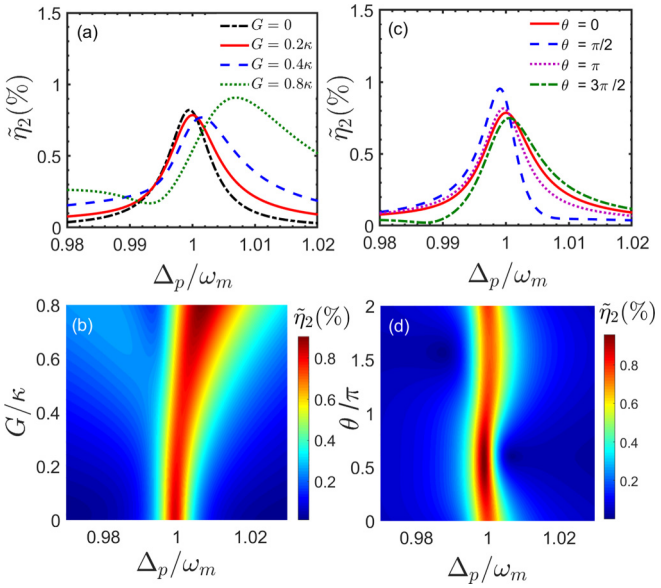

FIG. 10. Efficiency $\tilde{\eta}_2$ of the second-order lower sideband generation as a function of the probe-pulsed detuning Δ_p for different (a) nonlinear gain G for $\theta = 0$ and (c) phase θ of the field driving the OPA for $G = 0.2\kappa$. (b) Variation of $\tilde{\eta}_2$ with Δ_p and G for $\theta = 0$. (d) Variation of $\tilde{\eta}_2$ with Δ_p and θ for $G = 0.2\kappa$. The resonator is stationary ($\Omega = 0$). The other parameters are the same as in Fig. 2.

We obtain the amplitude of the sidebands, which are substituted into the efficiency of the second-order upper sideband $\tilde{\eta}_1 = |-\sqrt{\kappa_{ex}}\tilde{A}_2^+/\varepsilon_p|$ and second-order lower sideband $\tilde{\eta}_2 = |-\sqrt{\kappa_{ex}}\tilde{A}_2^-/\varepsilon_p|$. To illustrate the different influences on the second-order sidebands of the OPA excited by a pump drive of frequency $\omega_g = 2\omega_l$, the efficiency of the second-order upper sideband generation with the resonator stationary is investigated as a function of frequency Δ_p/ω_m in Fig. 9. As shown in Fig. 9(a), in the absence of the OPA, the efficiency $\tilde{\eta}_1$ possesses two near-symmetrical peaks and a local minimum near the resonance condition $\Delta_p/\omega_m = 1$. When $G \neq 0$, with the nonlinear gain G of the OPA increasing, the peak of efficiency $\tilde{\eta}_1$ decreases gradually. However, in the driven frequency Δ_p range away from the resonance condition $\Delta_p = \omega_m$, such as $\Delta_p > 1.01\omega_m$, the efficiency $\tilde{\eta}_1$ is enhanced. Moreover, it is noted that the larger the nonlinear gain G of the OPA is, the wider the linewidth of the suppressive windows of the efficiency $\tilde{\eta}_1$ is. Due to the presence of the OPA, the suppressive window will be asymmetric. The result can be applied to determine the excitation number of atoms and plays important roles in nonlinear media in the optical properties of the output field. Interestingly, when G increases to $G = 0.8\kappa$, a clear asymmetric linear pattern of the efficiency $\tilde{\eta}_1$ emerges, with a much larger peak at $\Delta_p = 1.01\omega_m$ than at $\Delta_p = 0.987\omega_m$. In Fig. 9(c) we show the efficiency $\tilde{\eta}_1$ for different phase θ of the field driving the OPA. We find that the phase θ amplifies the efficiency of the second-order sideband generation, so the peak of $\tilde{\eta}_1$ increases from 9.52% to 11.53% for $\theta = \pi/2$. This is due to the fact that the degenerate parametric amplifier is a phase-sensitive amplifier, where the phase relationship between the control laser and signal laser driving the degenerate parametric amplifier determines the direction of the energy flow, i.e., whether the signal light is effectively amplified or not. Figures 9(b) and 9(d) show $\tilde{\eta}_1$ as a function of the detuning Δ_p and phase θ of the field driving the OPA. We can see that the efficiency of the second-order sideband generation is sensitive to both the nonlinear gain G and phase θ changes of the OPA. When $\Delta_p \in (\omega_m, 1.02\omega_m)$, the influence of G and θ on the efficiency $\tilde{\eta}_1$ becomes more obvious. In particular, as shown in Fig. 9(d), it can be found that at $\theta \in (0, 1.28\pi)$, the efficiency $\tilde{\eta}_1$ is amplified. When $\theta = 0.64\pi$ and $\Delta_p = 1.003\omega_m$, $\tilde{\eta}_1$ obtains the maximum value 11.73%. Next we discuss the influence of the OPA on the second-order lower sideband efficiency $\tilde{\eta}_2$. In Figs. 10(a) and 10(c) we can see that both G and θ change the peak of $\tilde{\eta}_2$ [for detailed results refer to Figs. 10(b) and 10(d)]. As G increases, the position of the peak shifts to the right, i.e., a larger value of Δ_p is needed to bring $\tilde{\eta}_2$ to its maximum. In particular, when $G = 0.8\kappa$, $\tilde{\eta}_2$ appears as a local minimum at $\Delta_p = 0.993\omega_m$. As shown in Fig. 10(d), $\tilde{\eta}_2$ is amplified when $\theta \in (0, 1.14\pi)$, which obtains the maximum value of 0.95%. In general, when the pump laser frequency driving the OPA is $\omega_g = 2\omega_l$, the nonlinear gain G of the OPA is not significant for the amplification of the second-order upper and lower sidebands. Compared with the case where the pump laser frequency driving the OPA is $\omega_g = \omega_l + \omega_p$, G can change the linewidth of the suppressive window of $\tilde{\eta}_2$ and localization of the sideband efficiency maximum. As shown in Fig. 11, we discuss the influence of the OPA on the second-order upper sideband generation when the resonator is rotating. In Fig. 11(a) it can be seen that when the system is driven from the left-hand side ($\Omega = 20$ kHz), the increase of the nonlinear gain G of the OPA enhances the second-order sideband peak. However, the effect of the OPA in the transmission window (near $\Delta_p/\omega_m = 1$) is small, while at $\Delta_p/\omega_m < 0.996$ and $\Delta_p/\omega_m > 1.004$ the OPA has a significant enhancement effect. In Fig. 11(b) we find that when the system is driven from the right-hand side

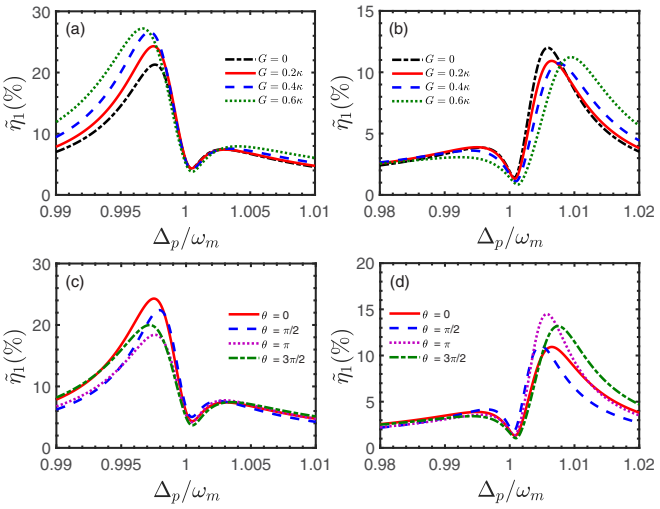

FIG. 11. Efficiency $\tilde{\eta}_1$ of the second-order upper sideband generation as a function of the probe-pulsed detuning Δ_p for different G with $\theta = 0$ at (a) $\Omega = 20$ kHz and (b) $\Omega = -20$ kHz and efficiency $\tilde{\eta}_1$ as a function of the probe-pulsed detuning Δ_p for different θ with $G = 0.2\kappa$ at (c) $\Omega = 20$ kHz and (d) $\Omega = -20$ kHz. The other parameters are the same as in Fig. 2.

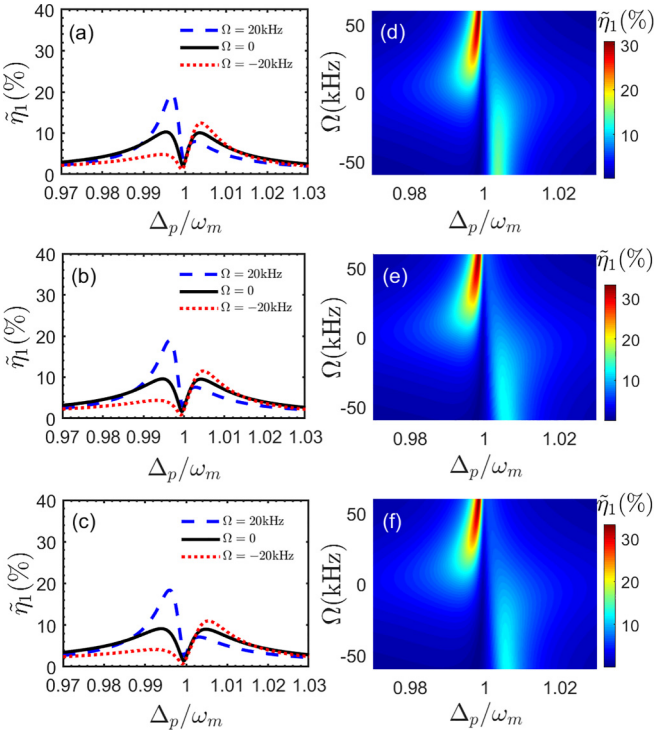

FIG. 12. Efficiency $\tilde{\eta}_1$ of the second-order upper sideband generation as a function of Δ_p for different values of Ω and incident directions of light, where the nonlinear gain and phase of the probe field of the OPA are fixed at (a) $G = 0$ and $\theta = 0$, (b) $G = 0.2\kappa$ and $\theta = 0$, and (c) $G = 0.2\kappa$ and $\theta = 3\pi/2$. The η_1 varies with Δ_p and Ω for different values (d) $G = 0$ and $\theta = 0$, (e) $G = 0.2\kappa$ and $\theta = 0$, and (f) $G = 0.2\kappa$ and $\theta = 3\pi/2$. These parameters are the same as in Fig. 2.

($\Omega = -20$ kHz), changing the nonlinear gain G cannot enhance the second-order sideband peak. However, the increase in the nonlinear gain G of the OPA still makes the linewidth of the efficiency $\tilde{\eta}_1$ broaden. In Figs. 11(c) and 11(d) $\tilde{\eta}_1$ is plotted as a function of detuning Δ_p for different θ at $G = 0.2\kappa$. In this case, $\Omega = 20$ and -20 kHz are fixed in Figs. 11(c) and 11(d), respectively. In detail, the second-order sideband peak is significantly enhanced when $\theta = \pi$ at $\Omega = -20$ kHz, but decreased at $\Omega = 20$ kHz.

In the above discussion, we note that when the frequency ω_g of the laser field driving the OPA is changed from $\omega_l + \omega_p$ to $2\omega_l$, the influence of the resonator speed, the direction of incidence of the input fields, the nonlinear gain of the OPA, and phase of the field driving the OPA on the second-order sideband efficiency is significantly different in the system. In Figs. 12 and 13 we find in such a hybrid nonlinear system containing the OPA that the spinning-induced direction-dependent nonreciprocal behavior remains. We fix the clockwise speed of the resonator at 20 kHz and vary the nonlinear gain G and phase θ of the field driving the OPA, plotting $\tilde{\eta}_1$ as a function of Δ_p and Ω when the spinning system is driven from the left-hand side and right-hand side, respectively. In Fig. 12 we choose the same OPA gain as in Fig. 2 to compare two different OPA cases ($\omega_g = \omega_l + \omega_p$ and $\omega_g = 2\omega_l$). When the control laser frequency driving the OPA is $\omega_g = 2\omega_l$, changing the nonlinear gain G cannot enhance the second-order sideband peak. The efficiency of the second-order upper sideband is not sensitive to the variation of the nonlinear gain of the OPA and phase of the field driving the OPA. It is interesting though that we can see that, with the resonator speed increasing, the second-order sideband peak shifts to the right regardless of the direction from which the system is driven, as shown in Figs. 12(e) and 12(f). Furthermore, there are also similarities between the two different OPA cases, such as, compared with the case where the system is driven from the right side ($\Omega < 0$), the influence of resonator rotation on the second-order sideband enhancement is much more significant when the system is driven from the left side ($\Omega > 0$).

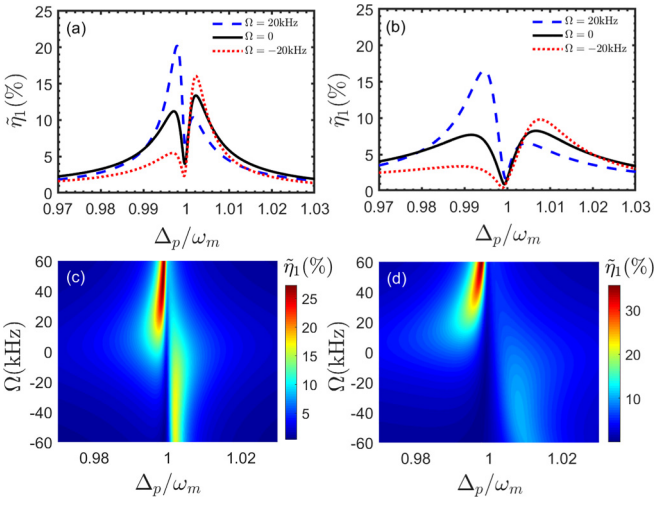

FIG. 13. (a) and (b) Efficiency $\tilde{\eta}_1$ of the second-order upper sideband generation as a function of Δ_p for different values of Ω and incident directions of light. (c) and (d) Variation of $\tilde{\eta}_1$ with Δ_p and Ω. The parameters are (a) and (c) $G = 0.4\kappa$ and $\theta = \pi/2$ and (b) and (d) $G = 0.4\kappa$ and $\theta = 3\pi/2$. The other parameters are the same as in Fig. 2.

VI. NONRECIPROCAL SECOND-ORDER SIDEBANDS IN NON-MARKOVIAN SYSTEMS

When the system interacts with the environment, the dynamics of the system is affected by the environment, that is, the dissipation or the backflow oscillation of the photon from the environment, where the former corresponds to the Markovian approximation, while the latter exhibits non-Markovian effects [107,113,157,158]. In Secs. II–V we studied the optomechanical second-order sidebands under the Markovian approximation. In this section we investigate the influence of non-Markovian effects on the efficiency of second-order sidebands. For this purpose, we consider that the cavity interacts with the non-Markovian environment consisting of a series of boson modes (eigenfrequency ω_k) [143–158], where the non-Markovian environment couples to an external reservoir. In a rotating frame defined by $\hat{U}_S(t) = \exp[-i\omega_l t(\hat{a}^\dagger\hat{a} + \sum_k \hat{b}_k^\dagger\hat{b}_k + \sum_j \hat{c}_j^\dagger\hat{c}_j)]$, the total Hamiltonian (5) is changed to

$$\begin{aligned}\hat{H}_{\rm eff} =& \hbar(\Delta_0 - \xi\hat{x} + \Delta_s)\hat{a}^\dagger\hat{a} + \frac{\hat{p}^2}{2m} + \frac{1}{2}m\omega_m^2\hat{x}^2 \\ &+ \frac{\hat{p}_\phi^2}{2m(R+\hat{x})^2} + i\hbar G(\hat{a}^{\dagger 2}e^{-i\Delta_p t}e^{i\theta} - \text{H.c.}) \\ &+ i\hbar\sqrt{\kappa_{ex}}[(\varepsilon_l + \varepsilon_p e^{-i\Delta_p t})\hat{a}^\dagger - \text{H.c.}] \\ &+ \hbar\sum_k \Delta_k\hat{b}_k^\dagger\hat{b}_k + i\hbar\sum_k (g_k\hat{a}\hat{b}_k^\dagger - \text{H.c.}) \\ &+ \hbar\sum_j (\tilde{\omega}_j - \omega_l)\hat{c}_j^\dagger\hat{c}_j + i\hbar\sum_{jk}(v_{jk}\hat{c}_j\hat{b}_k^\dagger - \text{H.c.}),\end{aligned} \tag{33}$$

where $\Delta_k = \omega_k - \omega_l$ defines the detuning of the kth mode (eigenfrequency ω_k) of the non-Markovian environment from the driving field, $\hat{b}_k$ ($\hat{b}_k^\dagger$) is the annihilation (creation) operator, g_k is the coupling coefficient between the cavity and environment, v_{jk} denotes the coupling strength between the kth mode of the non-Markovian environment and the jth mode of the external reservoir with frequency $\tilde{\omega}_j$, and $\hat{c}_j$ and $\hat{c}_j^\dagger$ represent annihilation and creation operators of the external reservoir, respectively. The dynamics of the system can be derived as

$$\begin{aligned}\frac{d}{dt}\hat{a}(t) =& -\left(\frac{\kappa}{2} + i(\Delta_0 - \xi\hat{x}(t) + \Delta_s)\right)\hat{a}(t) - \sum_k g_k^*\hat{b}_k(t) \\ &+ \sqrt{\kappa_{\rm ex}}(\varepsilon_l + \varepsilon_p e^{-i\Delta_p t}) + 2G\hat{a}^\dagger(t)e^{i\theta}e^{-i\Delta_p t},\end{aligned} \tag{34}$$

$$\frac{d}{dt}\hat{b}_k(t) = -i\Delta_k\hat{b}_k(t) + g_k\hat{a}(t) + \sum_j v_{jk}\hat{c}_j(t), \tag{35}$$

$$\frac{d}{dt}\hat{c}_j(t) = -i(\tilde{\omega}_j - \omega_l)\hat{c}_j(t) - \sum_{k_1} v_{jk_1}^*\hat{b}_{k_1}(t), \tag{36}$$

$$\frac{d^2}{dt^2}\hat{x}(t) + \Gamma_m\frac{d}{dt}\hat{x}(t) + \omega_m^2\hat{x}(t) = \frac{\hbar\xi}{m}\hat{a}^\dagger(t)\hat{a}(t) + \frac{\hat{p}_\phi^2(t)}{m^2R^3}, \tag{37}$$

$$\frac{d}{dt}\hat{\phi}(t) = \frac{\hat{p}_\phi(t)}{mR^2}, \tag{38}$$

$$\frac{d}{dt}\hat{p}_\phi(t) = 0, \tag{39}$$

with the intrinsic loss rate $\kappa_a = \kappa/2$ phenomenologically added in the above equations. Equation (36) gives

$$\begin{aligned}\hat{c}_j(t) =& e^{-i(\tilde{\omega}_j - \omega_l)t}\hat{c}_j(0) \\ &- \sum_{k_1} v_{jk_1}^*\int_0^t e^{-i(\tilde{\omega}_j - \omega_l)(t-\tau)}\hat{b}_{k_1}(\tau)d\tau.\end{aligned} \tag{40}$$

Substituting Eq. (40) into Eq. (35), we get

$$\begin{aligned}\frac{d}{dt}\hat{b}_k(t) =& -i\Delta_k\hat{b}_k(t) + g_k\hat{a}(t) + \sqrt{2\pi}c_{k,\rm in} \\ &- \sum_{k_1}\int_0^t D_{kk_1}(t-\tau)\hat{b}_{k_1}(\tau)d\tau,\end{aligned} \tag{41}$$

where the input-field operator of the reservoir $\hat{c}_{k,\rm in}(t) = \frac{1}{\sqrt{2\pi}}\sum_j v_{jk}e^{-i(\tilde{\omega}_j - \omega_l)t}\hat{c}_j(0)$, the correlation function $D_{kk_1}(t-\tau) = \sum_j v_{jk}v_{jk_1}^* e^{-i(\tilde{\omega}_j - \omega_l)(t-\tau)} = \int \tilde{J}_{kk_1}(\omega)e^{-i(\omega-\omega_l)(t-\tau)}d\omega$, and the spectral density of the reservoir $\tilde{J}_{kk_1}(\omega) = \sum_j v_{jk}v_{jk_1}^*\delta(\omega - \tilde{\omega}_j)$, with $\delta(\omega)$ the Dirac delta function. Taking $\tilde{J}_{kk_1}(\omega) = \frac{\mu_k}{\pi}\delta_{kk_1}$ (δ_{kk_1} represents the Kronecker delta symbol, i.e., $\delta_{kk_1} = 1$ for $k = k_1$ and $\delta_{kk_1} = 0$ otherwise) and then $D_{kk_1}(t-\tau) = 2\mu_k\delta(t-\tau)\delta_{kk_1}$ [107,178], we obtain

$$\frac{d}{dt}\hat{b}_k(t) = -i\tilde{\Delta}_k\hat{b}_k(t) + g_k\hat{a}(t) + \sqrt{2\pi}\hat{c}_{k,\rm in}, \tag{42}$$

with $\tilde{\Delta}_k = \Delta_k - i\mu_k$. To simplify the calculation, we assume $\mu_k \equiv \mu$ below, where μ denotes the decay from the non-Markovian environment coupling to an external reservoir. The solution of Eq. (42) is

$$\begin{aligned}\hat{b}_k(t) =& \hat{b}_k(0)e^{-i\tilde{\Delta}_k t} + g_k\int_0^t \hat{a}(\tau)e^{-i\tilde{\Delta}_k(t-\tau)}d\tau \\ &+ \sqrt{2\pi}\int_0^t \hat{c}_{k,\rm in}(\tau)e^{-i\tilde{\Delta}_k(t-\tau)}d\tau.\end{aligned} \tag{43}$$

The first term on the right-hand side of Eq. (43) represents the freely propagating parts of the environmental fields and the second term describes the influence of the non-Markovian environment on the cavity. The third term on the right-hand side of Eq. (43) denotes the influence of the input-field operator of the reservoir on the non-Markovian environment. Substituting Eq. (43) into Eq. (34), we obtain an integro-differential equation

$$\begin{aligned}\frac{d}{dt}\hat{a}(t) =& -\left(\frac{\kappa}{2} + i[\Delta_0 - \xi\hat{x}(t) + \Delta_s]\right)\hat{a}(t) \\ &+ \sqrt{\kappa_{\rm ex}}(\varepsilon_l + \varepsilon_p e^{-i\Delta_p t}) + 2G\hat{a}^\dagger(t)e^{i\theta}e^{-i\Delta_p t} \\ &+ \hat{K}(t) + \hat{L}(t) - \int_0^t \hat{a}(\tau)f(t-\tau)d\tau,\end{aligned} \tag{44}$$

where $\hat{K}(t) = -\sum_k g_k^*\hat{b}_k(0)e^{-i\tilde{\Delta}_k t} = \int_{-\infty}^{\infty} h^*(t-\tau)\hat{a}_{\rm in}(\tau)d\tau$, $\hat{L}(t) = -\sqrt{2\pi}\sum_k g_k^*\int_0^t \hat{c}_{k,\rm in}(\tau)e^{-i\tilde{\Delta}_k(t-\tau)}d\tau$, the input-field operator $\hat{a}_{\rm in}(t) = \frac{1}{\sqrt{2\pi}}\sum_k e^{-i\tilde{\Delta}_k t}\hat{b}_k(0)$, the impulse response function $h(t) = \frac{-1}{\sqrt{2\pi}}\sum_k e^{i\tilde{\Delta}_k t}g_k \equiv \frac{-1}{\sqrt{2\pi}}\int e^{i(\omega-\omega_l)t+\mu t}g(\omega)d\omega$ [we have made the replacement $g_k \to g(\omega)$ in the continuum limit], and the correlation function $f(t) = \sum_k |g_k|^2 e^{-i\tilde{\Delta}_k t} = \int J(\omega)e^{-i(\omega-\omega_l)t-\mu t}d\omega$, with the spectral density of the non-Markovian environment $J(\omega) = \sum_k |g_k|^2\delta(\omega - \omega_k)$. Both

$\hat{a}_{\rm in}(t)$ and $\hat{c}_{k,\rm in}$ are the input fields with zero expectation value $a_{\rm in}(t) = \langle \hat{a}_{\rm in}(t)\rangle = 0$ and $c_{k,\rm in}(t) = \langle \hat{c}_{k,\rm in}(t)\rangle = 0$ for the environment and reservoir initialization in the vacuum states, which lead to $K(t) = \langle \hat{K}(t)\rangle = 0$ and $L(t) = \langle \hat{L}(t)\rangle = 0$. We define the spectral response function as

$$g(\omega) = \sqrt{\frac{\kappa_{\rm ex}}{2\pi}}\frac{\lambda_1}{\lambda_1 - i(\omega-\omega_l)}, \tag{45}$$

where λ_1 is the environmental spectrum width and $\kappa_{\rm ex} = \kappa$ is the cavity dissipation through the input and output ports. The spectral density of the environment is [179–183]

$$J(\omega) = \frac{\kappa_{\rm ex}}{2\pi}\frac{\lambda_1^2}{\lambda_1^2 + (\omega-\omega_l)^2}, \tag{46}$$

which corresponds to the Lorentzian spectral density. With Eqs. (45) and (46) we get $h(\tau - t) = -\sqrt{\kappa_{\rm ex}}\lambda_1 e^{-(\lambda_1+i\mu)(t-\tau)}\theta(t-\tau)$ and $f(t-\tau) = \frac{1}{2}\kappa_{\rm ex}\lambda_1 e^{-(\lambda_1+i\mu)|t-\tau|}$, where $\theta(t-t')$ is the unit step function; $\theta(t-t') = 1$ for $t \geqslant t'$, which represents a Gaussian Ornstein-Uhlenbeck process [184–186]. For convenience, we take the expectation values of the operator equations by defining $a \equiv \langle \hat{a}\rangle$, $x \equiv \langle \hat{x}\rangle$, $\phi \equiv \langle \hat{\phi}\rangle$, and $p_\phi \equiv \langle \hat{p}_\phi\rangle$. The steady-state solution of the non-Markovian system can be obtained from Eq. (44) as

$$\begin{aligned} a'_s &= \frac{\sqrt{\kappa_{\rm ex}}\varepsilon_l}{\kappa + i\Delta'}, \\ x'_s &= \frac{\hbar\xi|a'_s|^2}{m\omega_m^2} + R\left(\frac{\Omega}{\omega_m}\right)^2, \end{aligned} \tag{47}$$

where $\Delta' = \Delta_0 - \xi x'_s + \Delta_s$. We make the ansatz

$$\begin{aligned} a &= a'_s + A'^{+}_1 e^{-i\Delta_p t} + A'^{-}_1 e^{i\Delta_p t} + A'^{+}_2 e^{-2i\Delta_p t} + A'^{-}_2 e^{2i\Delta_p t}, \\ x &= x'_s + X'^{+}_1 e^{-i\Delta_p t} + X'^{-}_1 e^{i\Delta_p t} + X'^{+}_2 e^{-2i\Delta_p t} + X'^{-}_2 e^{2i\Delta_p t}. \end{aligned}$$

We get the linear response of the probe field

$$\begin{aligned} \sigma'_1(\Delta_p)A'^{+}_1 &= \Lambda(\Delta_p)(i\xi a'_s X'^{+}_1 + 2Ge^{i\theta}a'^{*}_s + \sqrt{\kappa_{\rm ex}}\varepsilon_p), \\ \sigma'_2(\Delta_p)A'^{-*}_1 &= -i\xi\Lambda(\Delta_p)a'^{*}_s A'^{+}_1, \\ \chi(\Delta_p)X'^{+}_1 &= \hbar\xi(a'_s A'^{-*}_1 + a'^{*}_s A'^{+}_1) \end{aligned} \tag{48}$$

and second-order sideband process

$$\begin{aligned} \sigma'_1(2\Delta_p)A'^{+}_2 &= \Lambda(2\Delta_p)[i\xi(a'_s X'^{+}_2 + A'^{+}_1 X'^{+}_1) + 2Ge^{i\theta}A'^{-*}_1], \\ \sigma'_2(2\Delta_p)A'^{-*}_2 &= -i\xi\Lambda(2\Delta_p)(a'^{*}_s X'^{+}_2 + A'^{-*}_1 X'^{+}_1), \\ \chi(2\Delta_p)X'^{+}_2 &= \hbar\xi(a'^{*}_s A'^{+}_2 + a'_s A'^{-*}_2 + A'^{-*}_1 A'^{+}_1), \end{aligned} \tag{49}$$

with

$$\begin{aligned} \Lambda(n\Delta_p) &= \lambda_1 + i\mu - in\Delta_p, \\ \sigma'_1(n\Delta_p) &= \kappa\lambda_1 - \frac{i\kappa n\Delta_p}{2} + \Lambda(n\Delta_p)(i\Delta - in\Delta_p), \\ \sigma'_2(n\Delta_p) &= \kappa\lambda_1 - \frac{i\kappa n\Delta_p}{2} - \Lambda(n\Delta_p)(i\Delta + in\Delta_p), \\ \chi(n\Delta_p) &= m\left(\omega_m^2 - i\Gamma_m n\Delta_p - \Delta_p^2\right). \end{aligned} \tag{50}$$

Through the non-Markovian input-output relation derived by Eq. (44), we obtain the expected value of the output field

$$a_{\rm out}(t) = a_{\rm in}(t) + \int_0^t h(\tau - t)a(\tau)d\tau. \tag{51}$$

Thus, in the non-Markovian case, the efficiency of the second-order upper sideband is defined as

$$\eta'_1 = \left|-\frac{\sqrt{\kappa_{\rm ex}}\lambda_1 A'^{+}_2 \frac{1}{\lambda_1 + i\mu - 2i\Delta_p}}{\varepsilon_p}\right|. \tag{52}$$

With Eq. (52), we consider the following two cases separately.

(i) In the first case, we take the decay $\mu = 0$ in Eq. (52). In Fig. 14(a) with the decay $\mu = 0$ and the resonator stationary but without the participation of the OPA, we show the efficiency of second-order upper sideband generation as a function of Δ_p with different spectral widths of the environment λ_1. For a given spectral width of the environment, decreasing from $\lambda_1 = 10\omega_m$ to $\lambda_1 = 2\omega_m$, we find from the figure that the second-order upper sideband η'_1 gradually decreases and its two located peaks become increasingly asymmetric in the non-Markovian environment. Interestingly, from Fig. 14(b) with the decay $\mu = 0$, when the light comes from the right side and $\Omega = 7.7$ kHz, η'_1 becomes symmetric in the non-Markovian environment at $\lambda_1 = 2\omega_m$. In other words, by controlling the rotation speed of the resonator and incident direction of the input fields, the symmetry of the second-order sideband is restored, but with a change in height compared with the Markovian environment. With the purpose of seeing the influence of the environmental spectrum width on the second-order sideband generation more clearly, the efficiency η'_1 as a function of both Δ_p and λ_1 is shown in Figs. 14(c) and 14(d) with the decay $\mu = 0$.

As the spectrum width of the environment is further increased, the efficiency of second-order upper sideband generation increases. For the sake of clarity, we separately draw in Fig. 15 the non-Markovian case and the Markovian limit case where the environmental spectrum width $\lambda_1 = 200\omega_m$ for the condition that the resonator is stationary and no OPA is involved with the decay $\mu = 0$. This figure shows the consistency of the nonreciprocal second-order upper sideband between the non-Markovian limit with $\lambda_1 = 200\omega_m$ and the Markovian approximation, regardless of the incident direction of the input fields. This originates from the fact that the correlation function $f(t)$ and impulse response function $h(t)$ tend to $\kappa_{\rm ex}\delta(t)$ and $-\sqrt{\kappa_{\rm ex}}\delta(t)$ in the wideband limit (i.e., the spectrum width λ_1 approaches infinity), respectively, which leads to Eqs. (44) and (51) in the non-Markovian regime returning to Eqs. (6) and (16) under the Markovian approximation. Figures 16(a)–16(d), with decay $\mu = 0$, show the spinning-induced direction-dependent nonreciprocal behavior of the second-order upper sideband in the non-Markovian environment but without the participation of the OPA. We note that, on the one hand, the efficiency of the second-order sideband η'_1 is very sensitive to the environmental spectrum width. On the other hand, the operating bandwidth for observing an obvious nonreciprocal enhancement of second-order sideband changes in the non-Markovian environment. Compared with the Markovian environment in Fig. 15 with the decay $\mu = 0$, the operating bandwidth becomes significantly wider at frequency $\Delta_p > \omega_m$ and narrower at $\Delta_p < \omega_m$.

Figures 14–16, with decay $\mu = 0$, present the influence of a pure non-Markovian effect on the second-order sideband without the participation of the OPA ($G = 0$). In Fig. 17, with decay $\mu = 0$, we show the variation of second-order upper

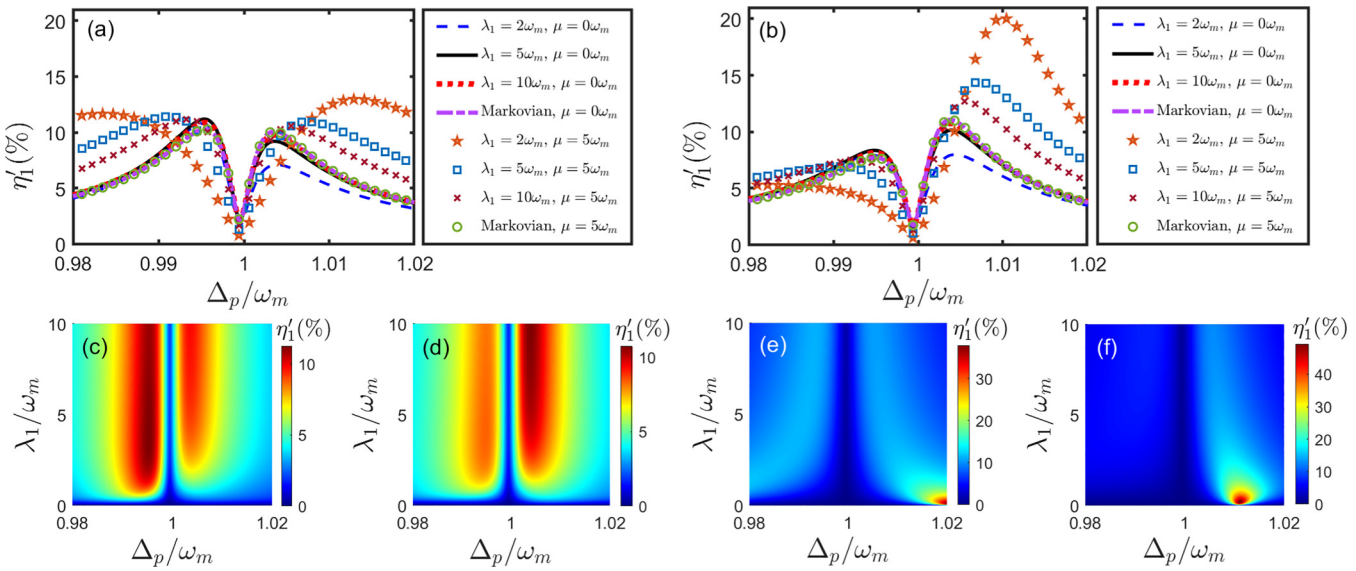

FIG. 14. (a) and (b) Efficiency η_1' of the second-order upper sideband generation as a function of Δ_p, which corresponds to the Markovian and non-Markovian environments with the different environmental spectrum width λ_1 without the OPA involvement ($G = 0$). (c)–(f) Variation of η_1' with Δ_p and λ_1. The rotation speed is set at (a), (c), and (e) $\Omega = 0$ and (b), (d), and (f) $\Omega = 7.7$ kHz. The parameter μ denotes the decay from the non-Markovian environment coupling to an external reservoir, where (c) and (d) $\mu = 0$ and (e) and (f) $\mu = 5\omega_m$. The other parameters are the same as in Fig. 2.

sideband efficiency in the presence of both the non-Markovian effect and the OPA. As expected, when the nonlinear gain G of the OPA increases from 0 to 0.6κ, the efficiency η_1' is significantly enhanced. Moreover, the non-Markovian effect is more pronounced for η_1' when the environmental spectrum width is small (i.e., $\lambda_1 < 2\omega_m$). As shown in Fig. 17(d), with decay $\mu = 0$ at $\lambda_1 = 30\omega_m$, the enhancement effect of the OPA for the second-order sideband is almost identical to the case of the Markovian limit.

(ii) In the second case, we take the decay $\mu = 5\omega_m$ in Eq. (52). The influences of the decay from the non-Markovian environment coupling to an external reservoir on the efficiency of second-order upper sidebands are shown in Figs. 14–16 with $\mu = 5\omega_m$. We find that the decay μ has a large influence on the efficiency of second-order upper sidebands in non-Markovian regimes, while it has almost no influence on the efficiency of second-order upper sidebands under the Markovian approximation. This is because the decay μ is comparable to the spectral width λ_1 of the non-Markovian environment revealed from Eqs. (50) and (52) [see Figs. 14(a), 14(b), 14(e), and 14(f) and Figs. 16(a), 16(b), 16(e), and 16(f)] since the spectral width λ_1 takes finite values in non-Markovian regimes. However, the spectral width λ_1 tends to infinity (i.e., $\lambda_1 \to \infty$) under the Markovian approximation, which leads to a decay μ that is negligible compared with the spectral width λ_1 due to $\mu \ll \infty$ in Eqs. (50) and (52) [see Figs. 14(a), 14(b), and 15].

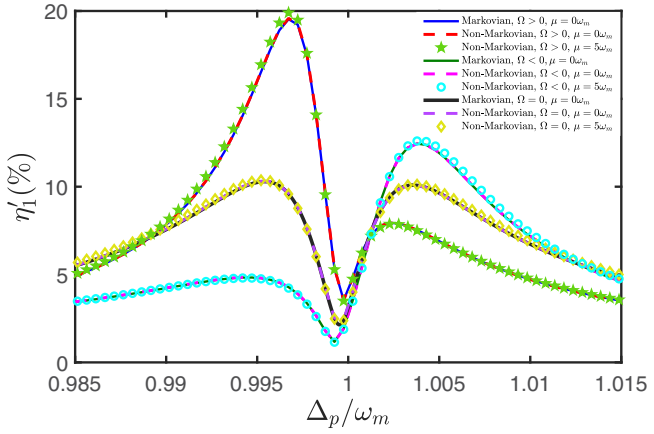

FIG. 15. Efficiency η_1' of the second-order upper sideband generation as a function of Δ_p for different values of Ω and incident directions of light, where we take $G = 0$. The consistency of nonreciprocal second-order sidebands is shown between the non-Markovian limit with $\lambda_1 = 200\omega_m$ and the Markovian approximation. The other parameters are the same as in Fig. 2.

VII. CONCLUSION

In summary, we have studied theoretically the second-order OMIT sidebands and group delays in a spinning resonator containing an optical parametric amplifier. We discussed the influence of the OPA driven by different pumping frequencies on the second-order sideband generation. The results show that the second-order sidebands in the rotating resonator can be greatly enhanced in the presence of the OPA and still maintain the nonreciprocal behavior due to the optical Sagnac effect. The second-order sidebands can be adjusted simultaneously by the pumping frequency and phase of the field driving the OPA, the gain coefficient of the OPA, the rotation speed of the resonator, and the incident direction of the input fields. When the OPA is excited by a pump driving with the frequency $\omega_g = \omega_l + \omega_p$, the higher the nonlinear gain of the OPA is, the stronger the second-order sidebands are. At this point, the OPA can only enhance the second-order sidebands but cannot change the position of the peaks and the nonreciprocal nature due to resonator rotation,

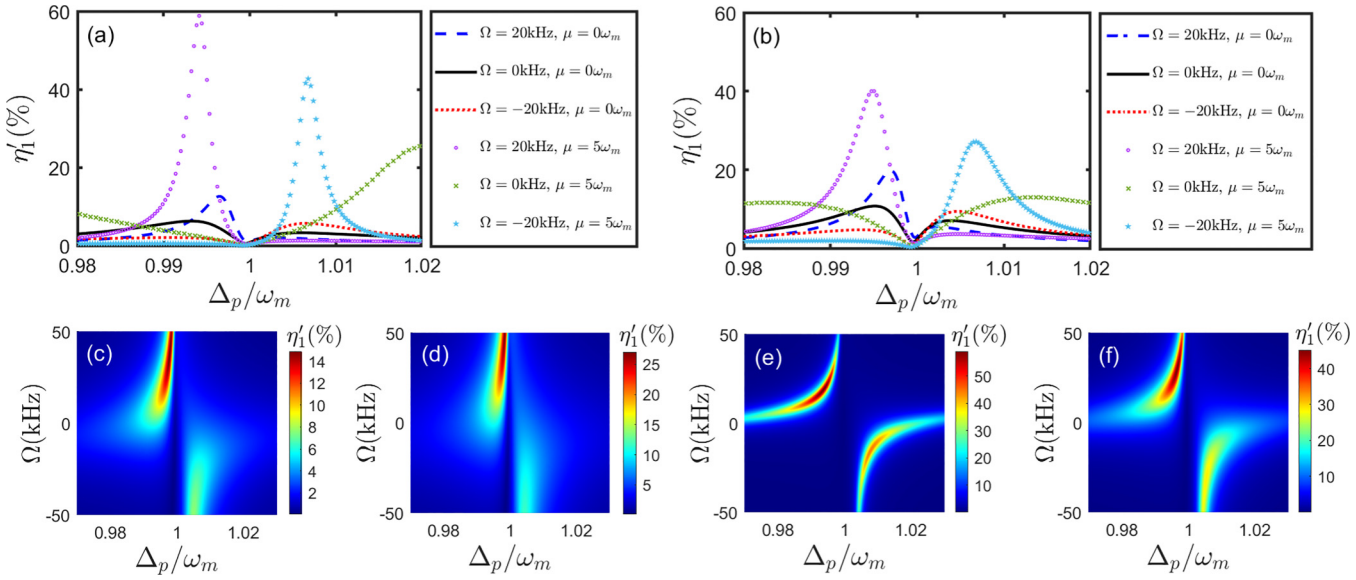

FIG. 16. (a) and (b) Efficiency η_1' of the second-order upper sideband generation as a function of Δ_p for different values of Ω and incident directions of light in the non-Markovian environment and without the participation of the OPA ($G = 0$). (c)–(f) Variation of η_1' with Δ_p and Ω. The environmental spectrum widths are (a), (c), and (e) $\lambda_1 = 0.5\omega_m$ and (b), (d), and (f) $\lambda_1 = 2\omega_m$. The decay (c) and (d) $\mu = 0$ and (e) and (f) $\mu = 5\omega_m$. The other parameters are the same as in Fig. 2.

which maintains the localization of the maximum value of the sideband efficiency. When the OPA is excited by a pump driving with the frequency $\omega_g = 2\omega_l$, the nonlinear gain of the OPA cannot enhance the second-order sidebands, which can only be achieved by adjusting the phase of the field driving the OPA. The OPA can also change the linewidth of the suppressive window of the second-order sidebands, which can be applied to determining the excitation number of atoms and plays important roles in nonlinear media in the optical properties of the output field. Combining the Sagnac transformation and the presence of the OPA, we demonstrated that the group delay of the second-order upper sideband can be tuned by adjusting the nonlinear gain and phase of the field driving the OPA, the rotation speed of the resonator, and incident direction of the input fields, which allowed us to realize a tunable switch from slow light to fast light in the spinning optomechanical system. Moreover, we extended the study of second-order sidebands from the Markovian to the non-Markovian bath, which consists of a collection of infinite oscillators (bosonic photonic modes). We found that the second-order OMIT sidebands in a spinning resonator exhibit a transition from the non-Markovian to the Markovian regime by controlling the environmental spectral width. Finally, we investigated the influence of the decay from the non-Markovian environment coupling to an external reservoir on the efficiency of second-order upper sidebands.

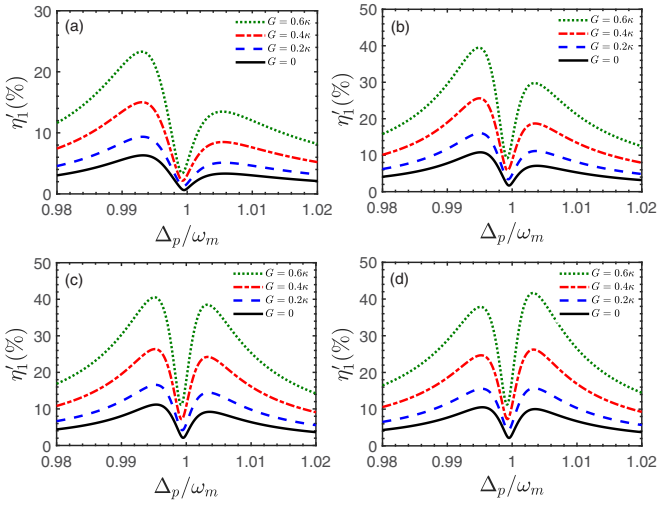

FIG. 17. Efficiency η_1' of the second-order upper sideband generation as a function of Δ_p for different nonlinear gain G of the OPA, where $\theta = 0$, $\Omega = 0$, and the decay $\mu = 0$. The environmental spectrum widths are (a) $\lambda_1 = 0.5\omega_m$, (b) $\lambda_1 = 2\omega_m$, (c) $\lambda_1 = 5\omega_m$, and (d) $\lambda_1 = 30\omega_m$. The other parameters are the same as in Fig. 2.

These results indicate the advantage of using a hybrid nonlinear system and contribute to a better understanding of light propagation in nonlinear optomechanical devices, which provides potential applications for precision measurement, optical communications, and quantum sensing. Expansions of the above non-Markovian nonreciprocal second-order sidebands to various general nonlinear physical models, e.g., (a) $\chi^{(2)}$ nonlinear materials $\hat{a}^2\hat{b}^\dagger + \hat{b}\hat{a}^{\dagger 2}$ [187,188], (b) Kerr nonlinear mediums $\hat{a}^{\dagger 2}\hat{a}^2$ [189,190], and (c) quadratic optomechanical systems $\hat{a}^\dagger\hat{a}(\hat{b} + \hat{b}^\dagger)^2$ [1,18,191–194], deserve further investigation.

ACKNOWLEDGMENTS

This work was supported by National Natural Science Foundation of China under Grant No. 12274064, Scientific Research Project for Department of Education of Jilin Province under Grant No. JJKH20190262KJ, and Natural Science Foundation of Jilin Province (subject arrangement project) under Grant No. 20210101406JC.

APPENDIX: DERIVATION OF EQS. (6)–(9)

In order to give the origin of Γ_m in Eq. (7), we add the coupling Hamiltonian $\hat{H}_{\rm cpl}$ [195–202] between the mechanical mode and a bosonic bath consisting of a set of harmonic oscillators with mass m_l and frequency Ω_l to Eq. (5) as

$$\hat{H}_{\rm cpl} = \sum_l \left[\frac{\hat{P}_l^2}{2M_l} + \frac{M_l\Omega_l^2}{2}\left(\hat{C}_l - \frac{v_l}{M_l\Omega_l^2}\hat{x}\right)^2\right], \tag{A1}$$

where $\hat{C}_l$ and $\hat{P}_l$ are the coordinate and momentum of the harmonic oscillators, respectively, and v_l denotes the coupling strength between the mechanical mode and bath. The counterterm proportional to $\hat{x}^2$ is typically introduced in the Hamiltonian, which accounts for a renormalization of the central oscillator frequency due to the interaction with the bath [195–202]. The Heisenberg equations read

$$\frac{d}{dt}\hat{a} = -[\kappa + i(\Delta_0 - \xi x + \Delta_s)]\hat{a} + \sqrt{\kappa_{\rm ex}}(\varepsilon_l + \varepsilon_p e^{-i\Delta_p t}) + 2G\hat{a}^\dagger e^{i\theta}e^{-i\Delta_p t}, \tag{A2}$$

$$\frac{d}{dt}\hat{x} = \frac{\hat{p}}{m}, \tag{A3}$$

$$\frac{d}{dt}\hat{p} = -m\omega_m^2\hat{x} + \sum_l v_l\hat{C}_l - \sum_l \frac{v_l^2}{M_l\Omega_l^2}\hat{x} + \hbar\xi\hat{a}^\dagger\hat{a} + \frac{\hat{p}_\phi^2}{mR^3}, \tag{A4}$$

$$\frac{d}{dt}\hat{C}_l = \frac{\hat{P}_l}{M_l}, \tag{A5}$$

$$\frac{d}{dt}\hat{P}_l = -M_l\Omega_l^2\hat{C}_l + v_l\hat{x}, \tag{A6}$$

$$\frac{d}{dt}\hat{\phi} = \frac{\hat{p}_\phi}{mR^2}, \tag{A7}$$

$$\frac{d}{dt}\hat{p}_\phi = 0, \tag{A8}$$

where the Heisenberg operator $\hat{x}(t)$ is abbreviated as $\hat{x} \equiv \hat{x}(t) = e^{i\hat{H}_T t/\hbar}\hat{x}(0)e^{i\hat{H}_T t/\hbar}$, with $\hat{H}_T = \hat{H}_{\rm eff} + \hat{H}_{\rm cpl}$ [$\hat{H}_{\rm eff}$ is given by Eq. (5)], and the other operators also have similar expressions. Equations (6), (8), and (9) are consistent with Eqs. (A2), (A7), and (A8), respectively. Differentiating Eqs. (A3) and (A5), together with Eqs. (A4) and (A6), we have

$$m\left(\frac{d^2}{dt^2}\hat{x} + \omega_m^2\hat{x}\right) = \sum_l v_l\hat{C}_l - \sum_l \frac{v_l^2}{M_l\Omega_l^2}\hat{x} + \hbar\xi\hat{a}^\dagger\hat{a} + \frac{\hat{p}_\phi^2}{mR^3}, \tag{A9}$$

$$\frac{d^2}{dt^2}\hat{C}_l + \Omega_l^2\hat{C}_l = \frac{v_l}{M_l}\hat{x}. \tag{A10}$$

The solution of Eq. (A10) is

$$\hat{C}_l = \hat{C}_l(0)\cos\Omega_l t + \frac{\hat{P}_l(0)}{M_l\Omega_l}\sin\Omega_l t + v_l\int_0^t \frac{\sin\Omega_l(t-\tau)}{M_l\Omega_l}\hat{x}(\tau)d\tau. \tag{A11}$$

Substituting Eq. (A11) into Eq. (A9) gives

$$m\left(\frac{d^2}{dt^2}\hat{x} + \omega_m^2\hat{x} + \int_0^t \eta(t-\tau)\hat{x}(\tau)d\tau\right) + \sum_l \frac{v_l^2}{M_l\Omega_l^2}\hat{x} = \hat{F}(t) + \hbar\xi\hat{a}^\dagger\hat{a} + \frac{\hat{p}_\phi^2}{mR^3}, \tag{A12}$$

with $\hat{F}(t) = \sum_l v_l\{\hat{C}_l(0)\cos\Omega_l t + [\hat{P}_l(0)/M_l\Omega_l]\sin\Omega_l t\}$. The kernel $\eta(t)$ equals $\frac{d\alpha(t)}{dt}$, where the correlation function $\alpha(t) = \sum_l v_l^2\cos\Omega_l t/mM_l\Omega_l^2 \equiv \int I(\omega)\cos(\omega)d\omega$, with the spectral density $I(\omega) = \sum_l \frac{v_l^2}{mM_l\Omega_l^2}\delta(\omega - \Omega_l)$. Taking expectation values (the states of each part for the system are initially prepared in their respective vacuum states) to Eq. (A12) leads to

$$m\left(\frac{d^2}{dt^2}x + \omega_m^2 x + \int_0^t \eta(t-\tau)x(\tau)d\tau\right) + \sum_l \frac{v_l^2}{M_l\Omega_l^2}x = \hbar\xi a^* a + \frac{p_\phi^2}{mR^3}, \tag{A13}$$

where we have used the expectation value $F(t) = \langle\hat{F}(t)\rangle$ of $\hat{F}(t)$ equaling zero. With the partial integration and $x(0) = 0$ [the expectation value of $\hat{x}(0)$ is $x(0) = \langle\hat{x}(0)\rangle$], Eq. (A13) is reduced as

$$m\left(\ddot{x} + \int_0^t \alpha(t-\tau)\dot{x}(\tau)d\tau + \omega_m^2 x\right) = \hbar\xi a^* a + \frac{p_\phi^2}{mR^3}. \tag{A14}$$

With the Lorentzian spectral density $I(\omega) = \Gamma_m\Lambda^2/\pi(\omega^2 + \Lambda^2)$ [107,113,157,158], we obtain $\alpha(t) = \Gamma_m\Lambda e^{-\Lambda|t|}$, where the parameter Λ defines the spectral width of the bath, which is connected to the bath correlation time T_B by the relation $T_B = \Lambda^{-1}$, while the timescale for the state of the system changing is given by $T_S = \Gamma_m^{-1}$. Under the Markovian approximation ($\Lambda \to \infty$), we get

$$\alpha(t) \to 2\Gamma_m\delta(t). \tag{A15}$$

Equation (7) can be obtained by substituting Eq. (A15) into Eq. (A14), where we have used the identity $\int_0^t \delta(t-\tau)\dot{x}(\tau)d\tau = \frac{1}{2}\dot{x}(t)$ [178].

[1] M. Aspelmeyer, T. J. Kippenberg, and F. Marquardt, Cavity optomechanics, Rev. Mod. Phys. **86**, 1391 (2014).

[2] M. Aspelmeyer, P. Meystre, and K. Schwab, Quantum optomechanics, Phys. Today **65**(7), 29 (2012).

[3] T. J. Kippenberg and K. J. Vahala, Cavity optomechanics: Back-action at the mesoscale, Science **321**, 1172 (2008).

[4] F. Marquardt and S. M. Girvin, Optomechanics, Physics **2**, 40 (2009).

[5] S. Sainadh U. and M. A. Kumar, Effects of linear and quadratic dispersive couplings on optical squeezing in an optomechanical system, Phys. Rev. A **92**, 033824 (2015).

[6] C. H. Metzger and K. Karrai, Cavity cooling of a microlever, Nature (London) **432**, 1002 (2004).

[7] S. Gigan, H. R. Böhm, M. Paternostro, F. Blaser, G. Langer, J. B. Hertzberg, K. C. Schwab, D. Bäuerle, M. Aspelmeyer, and A. Zeilinger, Self-cooling of a micromirror by radiation pressure, Nature (London) **444**, 67 (2006).

[8] A. Schliesser, O. Arcizet, R. Rivière, G. Anetsberger, and T. J. Kippenberg, Resolved-sideband cooling and position measurement of a micromechanical oscillator close to the Heisenberg uncertainty limit, Nat. Phys. **5**, 509 (2009).

[9] O. Arcizet, P. F. Cohadon, T. Briant, M. Pinard, and A. Heidmann, Radiation-pressure cooling and optomechanical instability of a micromirror, Nature (London) **444**, 71 (2006).

[10] P. Meystre, A short walk through quantum optomechanics, Ann. Phys. (Berlin) **525**, 215 (2013).

[11] A. Abramovici, W. E. Althouse, R. W. P. Drever, Y. Gürsel, S. Kawamura, F. J. Raab, D. Shoemaker, L. Sievers, R. E. Spero, K. S. Thorne, R. E. Vogt, R. Weiss, S. E. Whitcomb, and M. E. Zucker, LIGO: The laser interferometer gravitational-wave observatory, Science **256**, 325 (1992).

[12] C. M. Caves, Quantum-mechanical radiation-pressure fluctuations in an interferometer, Phys. Rev. Lett. **45**, 75 (1980).

[13] V. B. Braginsky and S. P. Vyatchanin, Low quantum noise tranquilizer for Fabry-Perot interferometer, Phys. Lett. A **293**, 228 (2002).

[14] A. A. Nejad, H. R. Askari, and H. R. Baghshahi, Optical bistability in coupled optomechanical cavities in the presence of Kerr effect, Appl. Opt. **56**, 2816 (2017); J. Y. Sun and H. Z. Shen, Photon blockade in non-Hermitian optomechanical systems with nonreciprocal couplings, Phys. Rev. A **107**, 043715 (2023).

[15] B. Sarma and A. K. Sarma, Controllable optical bistability in a hybrid optomechanical system, J. Opt. Soc. Am. B **33**, 1335 (2016).

[16] S. Shahidani, M. H. Naderi, M. Soltanolkotabi, and S. Barzanjeh, Steady-state entanglement, cooling, and tristability in a nonlinear optomechanical cavity, J. Opt. Soc. Am. B **31**, 1087 (2014).

[17] C. Jiang, Y. S. Cui, and K.-D. Zhu, Ultrasensitive nanomechanical mass sensor using hybrid opto-electromechanical systems, Opt. Express **22**, 13773 (2014).

[18] J. D. Thompson, B. M. Zwickl, A. M. Jayich, F. Marquardt, S. M. Girvin, and J. G. E. Harris, Strong dispersive coupling of a high-finesse cavity to a micromechanical membrane, Nature (London) **452**, 72 (2008).

[19] T. Bagci, A. Simonsen, S. Schmid, L. G. Villanueva, E. Zeuthen, J. Appel, J. M. Taylor, A. Sørensen, K. Usami, A. Schliesser, and E. S. Polzik, Optical detection of radio waves through a nanomechanical transducer, Nature (London) **507**, 81 (2014).

[20] R. W. Andrews, R. W. Peterson, T. P. Purdy, K. Cicak, R. W. Simmonds, C. A. Regal, and K. W. Lehnert, Bidirectional and efficient conversion between microwave and optical light, Nat. Phys. **10**, 321 (2014).

[21] A. A. Nejad, H. R. Askari, and H. R. Baghshahi, Optomechanical detection of weak microwave signals with the assistance of a plasmonic wave, Phys. Rev. A **97**, 053839 (2018).

[22] S. Weis, R. Rivière, S. Deléglise, E. Gavartin, O. Arcizet, A. Schliesser, and T. J. Kippenberg, Optomechanically induced transparency, Science **330**, 1520 (2010).

[23] A. H. Safavi-Naeini, T. P. M. Alegre, J. Chan, M. Eichenfield, M. Winger, Q. Lin, J. T. Hill, D. E. Chang, and O. Painter, Electromagnetically induced transparency and slow light with optomechanics, Nature (London) **472**, 69 (2011).

[24] W. Z. Jia, L. F. Wei, Y. Li, and Y.-X. Liu, Phase-dependent optical response properties in an optomechanical system by coherently driving the mechanical resonator, Phys. Rev. A **91**, 043843 (2015).

[25] H. Jing, Ş. K. Özdemir, Z. Geng, J. Zhang, X. Y. Lü, B. Peng, L. Yang, and F. Nori, Optomechanically-induced transparency in parity-time-symmetric microresonators, Sci. Rep. **5**, 9663 (2015).

[26] H. Wang, X. Gu, Y.-X. Liu, A. Miranowicz, and F. Nori, Optomechanical analog of two-color electromagnetically induced transparency: Photon transmission through an optomechanical device with a two-level system, Phys. Rev. A **90**, 023817 (2014).

[27] M. Karuza, C. Biancofiore, M. Bawaj, C. Molinelli, M. Galassi, R. Natali, P. Tombesi, G. Di Giuseppe, and D. Vitali, Optomechanically induced transparency in a membrane-in-the-middle setup at room temperature, Phys. Rev. A **88**, 013804 (2013).

[28] M. Fleischhauer, A. Imamoglu, and J. P. Marangos, Electromagnetically induced transparency: Optics in coherent media, Rev. Mod. Phys. **77**, 633 (2005).

[29] G. S. Agarwal and S. Huang, Electromagnetically induced transparency in mechanical effects of light, Phys. Rev. A **81**, 041803(R) (2010).

[30] D. E. Chang, A. H. Safavi-Naeini, M. Hafezi, and O. Painter, Slowing and stopping light using an optomechanical crystal array, New J. Phys. **13**, 023003 (2011).

[31] V. Fiore, Y. Yang, M. C. Kuzyk, R. Barbour, L. Tian, and H. Wang, Storing optical information as a mechanical excitation in a silica optomechanical resonator, Phys. Rev. Lett. **107**, 133601 (2011).

[32] X. Zhou, F. Hocke, A. Schliesser, A. Marx, H. Huebl, R. Gross, and T. J. Kippenberg, Slowing, advancing and switching of microwave signals using circuit nano-electromechanics, Nat. Phys. **9**, 179 (2013).

[33] J. T. Hill, A. H. Safavi-Naeini, J. Chan, and O. Painter, Coherent optical wavelength conversion via cavity optomechanics, Nat. Commun. **3**, 1196 (2012).

[34] S. Huang and G. S. Agarwal, Electromagnetically induced transparency with quantized fields in optocavity mechanics, Phys. Rev. A **83**, 043826 (2011).

[35] H. Xiong, L. Si, X. Lü, X. Yang, and Y. Wu, Review of cavity optomechanics in the weak-coupling regime: From linearization to intrinsic nonlinear interactions, Sci. China Phys. Mech. Astron. **58**, 1 (2015).

[36] N. Bartolo, F. Minganti, W. Casteels, and C. Ciuti, Exact steady state of a Kerr resonator with one- and two-photon driving and dissipation: Controllable Wigner-function multimodality and dissipative phase transitions, Phys. Rev. A **94**, 033841 (2016).

[37] Y. H. Zhou, S. S. Zhang, H. Z. Shen, and X. X. Yi, Second-order nonlinearity induced transparency, Opt. Lett. **42**, 1289 (2017).

[38] V. S. Ilchenko, A. A. Savchenkov, A. B. Matsko, and L. Maleki, Nonlinear optics and crystalline whispering gallery mode cavities, Phys. Rev. Lett. **92**, 043903 (2004).
[39] P. Rabl, Photon blockade effect in optomechanical systems, Phys. Rev. Lett. **107**, 063601 (2011).
[40] H. Flayac and V. Savona, Unconventional photon blockade, Phys. Rev. A **96**, 053810 (2017).
[41] M. A. Lemonde, N. Didier, and A. A. Clerk, Antibunching and unconventional photon blockade with Gaussian squeezed states, Phys. Rev. A **90**, 063824 (2014).
[42] F. Marino and F. Marin, Coexisting attractors and chaotic canard explosions in a slow-fast optomechanical system, Phys. Rev. E **87**, 052906 (2013).
[43] H. Xiong, L.-G. Si, A.-S. Zheng, X. Yang, and Y. Wu, Higher-order sidebands in optomechanically induced transparency, Phys. Rev. A **86**, 013815 (2012).
[44] L. Bi, J. Hu, P. Jiang, D. H. Kim, G. F. Dionne, L. C. Kimerling, and C. A. Ross, On-chip optical isolation in monolithically integrated non-reciprocal optical resonators, Nat. Photon. **5**, 758 (2011).
[45] P. Aleahmad, M. Khajavikhan, D. Christodoulides, and P. LiKamWa, Integrated multi-port circulators for unidirectional optical information transport, Sci. Rep. **7**, 2129 (2017).
[46] F. AbdelMalek, W. Aroua, S. Haxha, and I. Flint, Light-switching-light optical transistor based on metallic nanoparticle cross-chains geometry incorporating Kerr nonlinearity, Ann. Phys. (Berlin) **528**, 560 (2016).
[47] N. R. Bernier, L. D. Tóth, A. Koottandavida, M. A. Ioannou, D. Malz, A. Nunnenkamp, A. K. Feofanov, and T. J. Kippenberg, Nonreciprocal reconfigurable microwave optomechanical circuit, Nat. Commun. **8**, 604 (2017).
[48] H. Lü, Y. Jiang, Y.-Z. Wang, and H. Jing, Optomechanically induced transparency in a spinning resonator, Photon. Res. **5**, 367 (2017).
[49] L. Jin, J.-X. Peng, Q.-Z. Yuan, and X.-L. Fen, Macroscopic quantum coherence in a spinning optomechanical system, Opt. Express **29**, 41191 (2021).
[50] B. Li, R. Huang, X. Xu, A. Miranowicz, and H. Jing, Nonreciprocal unconventional photon blockade in a spinning optomechanical system, Photon. Res. **7**, 630 (2019).
[51] S. Maayani, R. Dahan, Y. Kligerman, E. Moses, A. U. Hassan, H. Jing, F. Nori, D. N. Christodoulides, and T. Carmon, Flying couplers above spinning resonators generate irreversible refraction, Nature (London) **558**, 569 (2018).
[52] Z. Shen, Y.-L. Zhang, Y. Chen, C.-L. Zou, Y.-F. Xiao, X.-B. Zou, F.-W. Sun, G.-C. Guo, and C.-H. Dong, Experimental realization of optomechanically induced non-reciprocity, Nat. Photonics **10**, 657 (2016).
[53] F. Ruesink, M. A. Miri, A. Alù, and E. Verhagen, Nonreciprocity and magnetic-free isolation based on optomechanical interactions, Nat. Commun. **7**, 13662 (2016).
[54] K. J. Fang, J. Luo, A. Metelmann, M. H. Matheny, F. Marquardt, A. A. Clerk, and O. Painter, Generalized non-reciprocity in an optomechanical circuit via synthetic magnetism and reservoir engineering, Nat. Phys. **13**, 465 (2017).
[55] Q.-T. Cao, H. Wang, C.-H. Dong, H. Jing, R.-S. Liu, X. Chen, L. Ge, Q. Gong, and Y.-F. Xiao, Experimental demonstration of spontaneous chirality in a nonlinear microresonator, Phys. Rev. Lett. **118**, 033901 (2017).
[56] W.-A. Li, G.-Y. Huang, J.-P. Chen, and Y. Chen, Nonreciprocal enhancement of optomechanical second-order sidebands in a spinning resonator, Phys. Rev. A **102**, 033526 (2020).
[57] H. Jing, H. Lü, Ş. K. Özdemir, T. Carmon, and F. Nori, Nanoparticle sensing with a spinning resonator, Optica **5**, 1424 (2018).
[58] H.-J. Chen, High-resolution biomolecules mass sensing based on a spinning optomechanical system with phonon pump, Appl. Phys. Express **14**, 082005 (2021).
[59] R. Huang, A. Miranowicz, J.-Q. Liao, F. Nori, and H. Jing, Nonreciprocal photon blockade, Phys. Rev. Lett. **121**, 153601 (2018).
[60] H. Xie, L.-W. He, X. Shang, G.-W. Lin, and X.-M. Lin, Nonreciprocal photon blockade in cavity optomagnonics, Phys. Rev. A **106**, 053707 (2022).
[61] Y. Jiang, S. Maayani, T. Carmon, F. Nori, and H. Jing, Nonreciprocal phonon laser, Phys. Rev. Appl. **10**, 064037 (2018).
[62] R. Peng, C. Zhao, Z. Yang, B. Xiong, and L. Zhou, Nonreciprocal amplification in coupled-rotating cavities around exceptional points, Ann. Phys. (Berlin) **533**, 2000405 (2021).
[63] H. L. Zhang, R. Huang, S.-D. Zhang, Y. Li, C.-W. Qiu, F. Nori, and H. Jing, Breaking anti-PT symmetry by spinning a resonator, Nano Lett. **20**, 7594 (2020).
[64] B. J. Li, Ş. K. Özdemir, X.-W. Xu, L. Zhang, L.-M. Kuang, and H. Jing, Nonreciprocal optical solitons in a spinning Kerr resonator, Phys. Rev. A **103**, 053522 (2021).
[65] S. Pina-Otey, F. Jiménez, P. Degenfeld-Schonburg, and C. Navarrete-Benlloch, Classical and quantum-linearized descriptions of degenerate optomechanical parametric oscillators, Phys. Rev. A **93**, 033835 (2016).
[66] G. Lin, A. Coillet, and Y. K. Chembo, Nonlinear photonics with high-Q whispering-gallery-mode resonators, Adv. Opt. Photon. **9**, 828 (2017).
[67] C.-S. Hu, L.-T. Shen, Z.-B. Yang, H. Wu, Y. Li, and S.-B. Zheng, Manifestation of classical nonlinear dynamics in optomechanical entanglement with a parametric amplifier, Phys. Rev. A **100**, 043824 (2019).
[68] H. H. Adamyan, J. A. Bergou, N. T. Gevorgyan, and G. Y. Kryuchkyan, Strong squeezing in periodically modulated optical parametric oscillators, Phys. Rev. A **92**, 053818 (2015).
[69] X.-Y. Lü, Y. Wu, J. R. Johansson, H. Jing, J. Zhang, and F. Nori, Squeezed optomechanics with phase-matched amplification and dissipation, Phys. Rev. Lett. **114**, 093602 (2015).
[70] X. Mi, J. Bai, and S. Ke-hui, Robust entanglement between a movable mirror and a cavity field system with an optical parametric amplifier, Eur. Phys. J. D **67**, 115 (2013).
[71] C.-S. Hu, X.-R. Huang, L.-T. Shen, Z.-B. Yang, and H.-Z. Wu, Enhancement of entanglement in distant micromechanical mirrors using parametric interactions, Eur. Phys. J. D **71**, 24 (2017).
[72] A. Xuereb, M. Barbieri, and M. Paternostro, Multipartite optomechanical entanglement from competing nonlinearities, Phys. Rev. A **86**, 013809 (2012).
[73] G. S. Agarwal and S. Huang, Strong mechanical squeezing and its detection, Phys. Rev. A **93**, 043844 (2016).
[74] S. Huang and G. S. Agarwal, Enhancement of cavity cooling of a micromechanical mirror using parametric interactions, Phys. Rev. A **79**, 013821 (2009).

[75] S. Huang and G. S. Agarwal, Normal-mode splitting in a coupled system of a nanomechanical oscillator and a parametric amplifier cavity, Phys. Rev. A **80**, 033807 (2009).

[76] B. Sarma and A. K. Sarma, Quantum-interference-assisted photon blockade in a cavity via parametric interactions, Phys. Rev. A **96**, 053827 (2017).

[77] H. Z. Shen, C. Shang, Y. H. Zhou, and X. X. Yi, Unconventional single-photon blockade in non-Markovian systems, Phys. Rev. A **98**, 023856 (2018).

[78] H. Z. Shen, Q. Wang, J. Wang, and X. X. Yi, Nonreciprocal unconventional photon blockade in a driven dissipative cavity with parametric amplification, Phys. Rev. A **101**, 013826 (2020).

[79] W. Qin, A. Miranowicz, P.-B. Li, X.-Y. Lü, J. Q. You, and F. Nori, Exponentially enhanced light-matter interaction, cooperativities, and steady-state entanglement using parametric amplification, Phys. Rev. Lett. **120**, 093601 (2018).

[80] M. A. Lemonde, N. Didier, and A. A. Clerk, Nonlinear interaction effects in a strongly driven optomechanical cavity, Phys. Rev. Lett. **111**, 053602 (2013).

[81] Y.-C. Liu, Y.-F. Xiao, Y.-L. Chen, X.-C. Yu, and Q. Gong, Parametric down-conversion and polariton pair generation in optomechanical systems, Phys. Rev. Lett. **111**, 083601 (2013).

[82] M. Mikkelsen, T. Fogarty, J. Twamley, and T. Busch, Optomechanics with a position-modulated Kerr-type nonlinear coupling, Phys. Rev. A **96**, 043832 (2017).

[83] T.-S. Yin, X.-Y. Lü, L.-L. Zheng, M. Wang, S. Li, and Y. Wu, Nonlinear effects in modulated quantum optomechanics, Phys. Rev. A **95**, 053861 (2017).

[84] H. Suzuki, E. Brown, and R. Sterling, Nonlinear dynamics of an optomechanical system with a coherent mechanical pump: Second-order sideband generation, Phys. Rev. A **92**, 033823 (2015).

[85] A. Kronwald and F. Marquardt, Optomechanically induced transparency in the nonlinear quantum regime, Phys. Rev. Lett. **111**, 133601 (2013).

[86] Y. Jiao, H. Lü, J. Qian, Y. Li, and H. Jing, Nonlinear optomechanics with gain and loss: Amplifying higher-order sideband and group delay, New J. Phys. **18**, 083034 (2016).

[87] S. P. Liu, W.-X. Yang, T. Shui, Z. Zhu, and A.-X. Chen, Tunable two-phonon higher-order sideband amplification in a quadratically coupled optomechanical system, Sci. Rep. **7**, 17637 (2017).

[88] L. R. Fan, K. Y. Fong, M. Poot, and H. X. Tang, Cascaded optical transparency in multimode-cavity optomechanical systems, Nat. Commun. **6**, 5850 (2015).

[89] H. Xiong, Z.-X. Liu, and Y. Wu, Highly sensitive optical sensor for precision measurement of electrical charges based on optomechanically induced difference-sideband generation, Opt. Lett. **42**, 3630 (2017).

[90] C. Kong, H. Xiong, and Y. Wu, Coulomb-interaction-dependent effect of high-order sideband generation in an optomechanical system, Phys. Rev. A **95**, 033820 (2017).

[91] J. D. Cohen, S. M. Meenehan, G. S. MacCabe, S. Gröblacher, A. H. Safavi-Naeini, F. Marsili, M. D. Shaw, and O. Painter, Phonon counting and intensity interferometry of a nanomechanical resonator, Nature (London) **520**, 522 (2015).

[92] K. Børkje, A. Nunnenkamp, J. D. Teufel, and S. M. Girvin, Signatures of nonlinear cavity optomechanics in the weak coupling regime, Phys. Rev. Lett. **111**, 053603 (2013).

[93] W. Zhao, S.-D. Zhang, A. Miranowicz, and H. Jing, Weak-force sensing with squeezed optomechanics, Sci. China Phys. Mech. Astron. **63**, 224211 (2020).

[94] Y. Li and K. Zhu, High-order sideband optical properties of a DNA-quantum dot hybrid system [Invited], Photon. Res. **1**, 16 (2013).

[95] Z. Zhang, Y.-P. Wang, and X. Wang, $\mathcal{PT}$-symmetry-breaking-enhanced cavity optomechanical magnetometry, Phys. Rev. A **102**, 023512 (2020); Z.-X. Liu, B. Wang, C. Kong, L.-G. Si, H. Xiong, and Y. Wu, A proposed method to measure weak magnetic field based on a hybrid optomechanical system, Sci. Rep. **7**, 12521 (2017).

[96] S. Liu, B. Liu, J. Wang, T. Sun, and W.-X. Yang, Realization of a highly sensitive mass sensor in a quadratically coupled optomechanical system, Phys. Rev. A **99**, 033822 (2019).

[97] B. Wang, Z.-X. Liu, H. Xiong, and Y. Wu, Highly sensitive mass sensing by means of the optomechanical nonlinearity, IEEE Photonics J. **10**, 6803908 (2018).

[98] S. P. Liu, W.-X. Yang, Z. H. Zhu, T. Shui, and L. Li, Quadrature squeezing of a higher-order sideband spectrum in cavity optomechanics, Opt. Lett. **43**, 9 (2018).

[99] R. W. Boyd and D. J. Gauthier, Controlling the velocity of light pulses, Science **326**, 1074 (2009).

[100] Y.-F. Jiao, T.-X. Lu, and H. Jing, Optomechanical second-order sidebands and group delays in a Kerr resonator, Phys. Rev. A **97**, 013843 (2018).

[101] Q. He, F. Badshah, R. U. Din, H. Zhang, Y. Hu, and G.-Q. Ge, Optomechanically induced transparency and the long-lived slow light in a nonlinear system, J. Opt. Soc. Am. B **35**, 1649 (2018).

[102] L. Li, W. Nie, and A. Chen, Transparency and tunable slow and fast light in a nonlinear optomechanical cavity, Sci. Rep. **6**, 35090 (2016).

[103] I. M. Mirza, W. Ge, and H. Jing, Optical nonreciprocity and slow light in coupled spinning optomechanical resonators, Opt. Express **27**, 25515 (2019).

[104] Q. Liao, W. Bao, X. Xiao, W. Nie, and Y. Liu, Optomechanically induced transparency and slow-fast light effect in hybrid cavity optomechanical systems, Crystals **11**, 698 (2021).

[105] F. Zimmer and M. Fleischhauer, Sagnac interferometry based on ultraslow polaritons in cold atomic vapors, Phys. Rev. Lett. **92**, 253201 (2004).

[106] M. S. Shahriar, G. S. Pati, R. Tripathi, V. Gopal, M. Messall, and K. Salit, Ultrahigh enhancement in absolute and relative rotation sensing using fast and slow light, Phys. Rev. A **75**, 053807 (2007).

[107] H.-P. Breuer and F. Petruccione, *The Theory of Open Quantum Systems* (Oxford University Press, Oxford, 2002).

[108] D. F. Walls and G. J. Milburn, *Quantum Optics* (Springer, Berlin, 1994).

[109] K. W. Chang and C. K. Law, Non-Markovian master equation for a damped oscillator with time-varying parameters, Phys. Rev. A **81**, 052105 (2010).

[110] H.-T. Tan and W.-M. Zhang, Non-Markovian dynamics of an open quantum system with initial system-reservoir correlations: A nanocavity coupled to a coupled-resonator optical waveguide, Phys. Rev. A **83**, 032102 (2011).

[111] S. Longhi, Non-Markovian decay and lasing condition in an optical microcavity coupled to a structured reservoir, Phys. Rev. A **74**, 063826 (2006).

[112] A. J. Leggett, S. Chakravarty, A. T. Dorsey, M. P. A. Fisher, A. Garg, and W. Zwerger, Dynamics of the dissipative two-state system, Rev. Mod. Phys. **59**, 1 (1987).

[113] H.-P. Breuer, E.-M. Laine, and J. Piilo, Measure for the degree of non-Markovian behavior of quantum processes in open systems, Phys. Rev. Lett. **103**, 210401 (2009).

[114] E.-M. Laine, J. Piilo, and H.-P. Breuer, Measure for the non-Markovianity of quantum processes, Phys. Rev. A **81**, 062115 (2010).

[115] C. Addis, B. Bylicka, D. Chruściński, and S. Maniscalco, Comparative study of non-Markovianity measures in exactly solvable one- and two-qubit models, Phys. Rev. A **90**, 052103 (2014).

[116] S. Wißmann, A. Karlsson, E.-M. Laine, J. Piilo, and H.-P. Breuer, Optimal state pairs for non-Markovian quantum dynamics, Phys. Rev. A **86**, 062108 (2012).

[117] S. Wißmann, H.-P. Breuer, and B. Vacchini, Generalized trace-distance measure connecting quantum and classical non-Markovianity, Phys. Rev. A **92**, 042108 (2015); L. Xin, S. Xu, X. X. Yi, and H. Z. Shen, Tunable nonMarkovian dynamics with a three-level atom mediated by the classical laser in a semi-infinite photonic waveguide, *ibid.* **105**, 053706 (2022).

[118] H. Z. Shen, D. X. Li, S.-L. Su, Y. H. Zhou, and X. X. Yi, Exact non-Markovian dynamics of qubits coupled to two interacting environments, Phys. Rev. A **96**, 033805 (2017); H. Z. Shen, Y. Chen, T. Z. Luan, and X. X. Yi, Multiple single-photon generations in three-level atoms coupled to a cavity with non-Markovian effects, *ibid.* **107**, 053705 (2023).

[119] S. Lorenzo, F. Plastina, and M. Paternostro, Geometrical characterization of non-Markovianity, Phys. Rev. A **88**, 020102(R) (2013).

[120] Á. Rivas, S. F. Huelga, and M. B. Plenio, Entanglement and non-Markovianity of quantum evolutions, Phys. Rev. Lett. **105**, 050403 (2010); H. Z. Shen, Q. Wang, and X. X. Yi, Dispersive readout with non-Markovian environments, Phys. Rev. A **105**, 023707 (2022).

[121] S. Luo, S. Fu, and H. Song, Quantifying non-Markovianity via correlations, Phys. Rev. A **86**, 044101 (2012).

[122] M. M. Wolf, J. Eisert, T. S. Cubitt, and J. I. Cirac, Assessing non-Markovian quantum dynamics, Phys. Rev. Lett. **101**, 150402 (2008).

[123] X.-M. Lu, X. Wang, and C. P. Sun, Quantum Fisher information flow and non-Markovian processes of open systems, Phys. Rev. A **82**, 042103 (2010).

[124] D. Chruściński and S. Maniscalco, Degree of non-Markovianity of quantum evolution, Phys. Rev. Lett. **112**, 120404 (2014).

[125] H. Z. Shen, S. Xu, H. T. Cui, and X. X. Yi, Non-Markovian dynamics of a system of two-level atoms coupled to a structured environment, Phys. Rev. A **99**, 032101 (2019); W.-Z. Zhang, J. Cheng, W.-D. Li, and L. Zhou, Optomechanical cooling in the non-Markovian regime, *ibid.* **93**, 063853 (2016).

[126] W.-Z. Zhang, Y. Han, B. Xiong, and L. Zhou, Optomechanical force sensor in a non-Markovian regime, New J. Phys. **19**, 083022 (2017).

[127] B. Xiong, X. Li, S.-L. Chao, and L. Zhou, Optomechanical quadrature squeezing in the non-Markovian regime, Opt. Lett. **43**, 6053 (2018).

[128] H. Z. Shen, S. L. Su, Y. H. Zhou, and X. X. Yi, Non-Markovian quantum Brownian motion in one dimension in electric fields, Phys. Rev. A **97**, 042121 (2018); X. Zhao, Macroscopic entanglement in optomechanical system induced by non-Markovian environment, Opt. Express **27**, 29082 (2019).

[129] J. F. Triana, A. F. Estrada, and L. A. Pachón, Ultrafast optimal sideband cooling under non-Markovian evolution, Phys. Rev. Lett. **116**, 183602 (2016).

[130] J. Cheng, X.-T. Liang, W.-Z. Zhang, and X. Duan, Optomechanical state transfer in the presence of non-Markovian environments, Opt. Commun. **430**, 385 (2019).

[131] H. Z. Shen, S. Xu, S. Yi, and X. X. Yi, Controllable dissipation of a qubit coupled to an engineering reservoir, Phys. Rev. A **98**, 062106 (2018); J. Cheng, W.-Z. Zhang, L. Zhou, and W. Zhang, Preservation macroscopic entanglement of optomechanical systems in non-Markovian environment, Sci. Rep. **6**, 23678 (2016).

[132] Q. Mu, H. Li, X. Huang, and X. Zhao, Microscopic-macroscopic entanglement transfer in optomechanical system: Non-Markovian effects, Opt. Commun. **426**, 70 (2018).

[133] X. Li, B. Xiong, S. Chao, and L. Zhou, Improving the sensitivity of weak microwave signal detection with optomechanical system under non-Markovian regime, J. Opt. Soc. Am. B **36**, 1363 (2019).

[134] Q. Ding, P. Zhao, Y. Ma, and Y. Chen, Impact of the central frequency of environment on non-Markovian dynamics in piezoelectric optomechanical devices, Sci. Rep. **11**, 1814 (2021).

[135] K. Sinha, P. Meystre, E. A. Goldschmidt, F. K. Fatemi, S. L. Rolston, and P. Solano, Non-Markovian collective emission from macroscopically separated emitters, Phys. Rev. Lett. **124**, 043603 (2020).

[136] W. Wu, S.-Y. Bai, and J.-H. An, Non-Markovian sensing of a quantum reservoir, Phys. Rev. A **103**, L010601 (2021).

[137] H. Z. Shen, X. Q. Shao, G. C. Wang, X. L. Zhao, and X. X. Yi, Quantum phase transition in a coupled two-level system embedded in anisotropic three-dimensional photonic crystals, Phys. Rev. E **93**, 012107 (2016); Q. Mu, X. Zhao, and T. Yu, Memory-effect-induced macroscopic-microscopic entanglement, Phys. Rev. A **94**, 012334 (2016).

[138] F. Caruso, V. Giovannetti, C. Lupo, and S. Mancini, Quantum channels and memory effects, Rev. Mod. Phys. **86**, 1203 (2014).

[139] A. D'Arrigo, R. Lo Franco, G. Benenti, E. Paladino, and G. Falci, Recovering entanglement by local operations, Ann. Phys. (NY) **350**, 211 (2014).

[140] R. Lo Franco, A. D'Arrigo, G. Falci, G. Compagno, and E. Paladino, Preserving entanglement and nonlocality in solid-state qubits by dynamical decoupling, Phys. Rev. B **90**, 054304 (2014).

[141] B. Bylicka, D. Chruściński, and S. Maniscalco, Non-Markovianity and reservoir memory of quantum channels: A quantum information theory perspective, Sci. Rep. **4**, 5720 (2014).

[142] S.-B. Xue, R.-B. Wu, W.-M. Zhang, J. Zhang, C.-W. Li, and T.-J. Tarn, Decoherence suppression via non-Markovian coherent feedback control, Phys. Rev. A **86**, 052304 (2012).

[143] B.-H. Liu, L. Li, Y.-F. Huang, C.-F. Li, G.-C. Guo, E.-M. Laine, H.-P. Breuer, and J. Piilo, Experimental control of the transition from Markovian to non-Markovian dynamics of open quantum systems, Nat. Phys. **7**, 931 (2011).

[144] S. Gröblacher, A. Trubarov, N. Prigge, G. D. Cole, M. Aspelmeyer, and J. Eisert, Observation of non-Markovian micromechanical Brownian motion, Nat. Commun. **6**, 7606 (2015).

[145] S.-J. Xiong, Q. Hu, Z. Sun, L. Yu, Q. Su, J.-M. Liu, and C.-P. Yang, Non-Markovianity in experimentally simulated quantum channels: Role of counterrotating-wave terms, Phys. Rev. A **100**, 032101 (2019).

[146] S. Cialdi, C. Benedetti, D. Tamascelli, S. Olivares, M. G. A. Paris, and B. Vacchini, Experimental investigation of the effect of classical noise on quantum non-Markovian dynamics, Phys. Rev. A **100**, 052104 (2019).

[147] D. Khurana, B. K. Agarwalla, and T. S. Mahesh, Experimental emulation of quantum non-Markovian dynamics and coherence protection in the presence of information backflow, Phys. Rev. A **99**, 022107 (2019).

[148] K. H. Madsen, S. Ates, T. Lund-Hansen, A. Löffler, S. Reitzenstein, A. Forchel, and P. Lodahl, Observation of non-Markovian dynamics of a single quantum dot in a micropillar cavity, Phys. Rev. Lett. **106**, 233601 (2011).

[149] Y. Guo, P. Taranto, B.-H. Liu, X.-M. Hu, Y.-F. Huang, C.-F. Li, and G.-C. Guo, Experimental demonstration of instrument-specific quantum memory effects and non-Markovian process recovery for common-cause processes, Phys. Rev. Lett. **126**, 230401 (2021).

[150] B.-W. Li, Q.-X. Mei, Y.-K. Wu, M.-L. Cai, Y. Wang, L. Yao, Z.-C. Zhou, and L.-M. Duan, Observation of non-Markovian spin dynamics in a Jaynes-Cummings-Hubbard model using a trapped-ion quantum simulator, Phys. Rev. Lett. **129**, 140501 (2022).

[151] U. Hoeppe, C. Wolff, J. Küchenmeister, J. Niegemann, M. Drescher, H. Benner, and K. Busch, Direct observation of non-Markovian radiation dynamics in 3D bulk photonic crystals, Phys. Rev. Lett. **108**, 043603 (2012).

[152] J.-S. Xu, C.-F. Li, C.-J. Zhang, X.-Y. Xu, Y.-S. Zhang, and G.-C. Guo, Experimental investigation of the non-Markovian dynamics of classical and quantum correlations, Phys. Rev. A **82**, 042328 (2010).

[153] J.-S. Tang, C.-F. Li, Y.-L. Li, X.-B. Zou, G.-C. Guo, H.-P. Breuer, E.-M. Laine, and J. Piilo, Measuring non-Markovianity of processes with controllable system-environment interaction, Europhys. Lett. **97**, 10002 (2012).

[154] S. A. Uriri, F. Wudarski, I. Sinayskiy, F. Petruccione, and M. S. Tame, Experimental investigation of Markovian and non-Markovian channel addition, Phys. Rev. A **101**, 052107 (2020).

[155] M. H. Anderson, G. Vemuri, J. Cooper, P. Zoller, and S. J. Smith, Experimental study of absorption and gain by two-level atoms in a time-delayed non-Markovian optical field, Phys. Rev. A **47**, 3202 (1993).

[156] Z.-D. Liu, Y.-N. Sun, B.-H. Liu, C.-F. Li, G.-C. Guo, S. Hamedani Raja, H. Lyyra, and J. Piilo, Experimental realization of high-fidelity teleportation via a non-Markovian open quantum system, Phys. Rev. A **102**, 062208 (2020).

[157] H.-P. Breuer, E.-M. Laine, J. Piilo, and B. Vacchini, *Colloquium*: Non-Markovian dynamics in open quantum systems, Rev. Mod. Phys. **88**, 021002 (2016).

[158] I. de Vega and D. Alonso, Dynamics of non-Markovian open quantum systems, Rev. Mod. Phys. **89**, 015001 (2017).

[159] C. C. Gerry and P. L. Knight, *Introductory Quantum Optics* (Cambridge University Press, Cambridge, 2005).

[160] W.-A. Li and G.-Y. Huang, Enhancement of optomechanically induced sum sidebands using parametric interactions, Phys. Rev. A **100**, 023838 (2019).

[161] P. D. Nation, J. R. Johansson, M. P. Blencowe, and F. Nori, *Colloquium*: Stimulating uncertainty: Amplifying the quantum vacuum with superconducting circuits, Rev. Mod. Phys. **84**, 1 (2012).

[162] Z. Leghtas, S. Touzard, I. M. Pop, A. Kou, B. Vlastakis, A. Petrenko, K. M. Sliwa, A. Narla, S. Shankar, M. J. Hatridge, M. Reagor, L. Frunzio, R. J. Schoelkopf, M. Mirrahimi, and M. H. Devoret, Confining the state of light to a quantum manifold by engineered two-photon loss, Science **347**, 853 (2015).

[163] A. A. Clerk, M. H. Devoret, S. M. Girvin, F. Marquardt, and R. J. Schoelkopf, Introduction to quantum noise, measurement, and amplification, Rev. Mod. Phys. **82**, 1155 (2010).

[164] S. Shen, Y. Qu, J. Li, and Y. Wu, Tunable photon statistics in parametrically amplified photonic molecules, Phys. Rev. A **100**, 023814 (2019).

[165] E. J. Post, Sagnac effect, Rev. Mod. Phys. **39**, 475 (1967).

[166] G. B. Malykin, The Sagnac effect: Correct and incorrect explanations, Phys. Usp. **43**, 1229 (2000).

[167] S. Huang and G. S. Agarwal, Robust force sensing for a free particle in a dissipative optomechanical system with a parametric amplifier, Phys. Rev. A **95**, 023844 (2017).

[168] M. O. Scully and M. S. Zubairy, *Quantum Optics* (Cambridge University Press, Cambridge, 1997).

[169] S. Davuluri and S. Y. Zhu, Controlling optomechanically induced transparency through rotation, Europhys. Lett. **112**, 64002 (2015).

[170] S. Shahidani, M. H. Naderi, and M. Soltanolkotabi, Control and manipulation of electromagnetically induced transparency in a nonlinear optomechanical system with two movable mirrors, Phys. Rev. A **88**, 053813 (2013).

[171] A. F. Adiyatullin, M. D. Anderson, H. Flayac, M. T. Portella-Oberli, F. Jabeen, C. Ouellet-Plamondon, G. C. Sallen, and B. Deveaud, Periodic squeezing in a polariton Josephson junction, Nat. Commun. **8**, 1329 (2017).

[172] J. D. Teufel, D. Li, M. S. Allman, K. Cicak, A. J. Sirois, J. D. Whittaker, and R. W. Simmonds, Circuit cavity electromechanics in the strong-coupling regime, Nature (London) **471**, 204 (2011).

[173] T.-X. Lu, X. Xiao, L.-S. Chen, Q. Zhang, and H. Jing, Magnon-squeezing-enhanced slow light and second-order sideband in cavity magnomechanics, Phys. Rev. A **107**, 063714 (2023).

[174] S.-N. Huai, Y.-L. Liu, J. Zhang, L. Yang, and Y.-x. Liu, Enhanced sideband responses in a $\mathcal{PT}$-symmetric-like cavity magnomechanical system, Phys. Rev. A **99**, 043803 (2019).

[175] P. W. Milonni, *Fast Light, Slow Light and Lefthanded Light* (Institute of Physics, Bristol, 2005).

[176] X. Zhang, Q.-T. Cao, Z. Wang, Y.-X. Liu, C.-W. Qiu, L. Yang, Q. Gong, and Y.-F. Xiao, Symmetry-breaking-induced nonlinear optics at a microcavity surface, Nat. Photon. **13**, 21 (2019).

[177] G. C. Righini, Y. Dumeige, P. Féron, M. Ferrari, G. N. Conti, D. Ristic, and S. Soria, Whispering gallery mode

microresonators: Fundamentals and applications, Riv. Nuovo Cimento **34**, 435 (2011).
[178] C. W. Gardiner and P. Zoller, *Quantum Noise* (Springer, Berlin, 2000).
[179] H. Z. Shen, M. Qin, and X. X. Yi, Single-photon storing in coupled non-Markovian atom-cavity system, Phys. Rev. A **88**, 033835 (2013).
[180] J. Zhang, Y.-x. Liu, R.-B. Wu, K. Jacobs, and F. Nori, Non-Markovian quantum input-output networks, Phys. Rev. A **87**, 032117 (2013).
[181] L. Diósi, Non-Markovian open quantum systems: Input-output fields, memory, and monitoring, Phys. Rev. A **85**, 034101 (2012).
[182] H.-N. Xiong, W.-M. Zhang, M. W.-Y. Tu, and D. Braun, Dynamically stabilized decoherence-free states in non-Markovian open fermionic systems, Phys. Rev. A **86**, 032107 (2012).
[183] H. Z. Shen, D. X. Li, and X. X. Yi, Non-Markovian linear response theory for quantum open systems and its applications, Phys. Rev. E **95**, 012156 (2017); H. Z. Shen, M. Qin, X. Q. Shao, and X. X. Yi, General response formula and application to topological insulator in quantum open system, *ibid.* **92**, 052122 (2015).
[184] G. E. Uhlenbeck and L. S. Ornstein, On the theory of the Brownian motion, Phys. Rev. **36**, 823 (1930).
[185] D. T. Gillespie, Exact numerical simulation of the Ornstein-Uhlenbeck process and its integral, Phys. Rev. E **54**, 2084 (1996).
[186] J. Jing and T. Yu, Non-Markovian relaxation of a three-level system: Quantum trajectory approach, Phys. Rev. Lett. **105**, 240403 (2010).
[187] A. Majumdar and D. Gerace, Single-photon blockade in doubly resonant nanocavities with second-order nonlinearity, Phys. Rev. B **87**, 235319 (2013).
[188] H. Z. Shen, Y. H. Zhou, and X. X. Yi, Quantum optical diode with semiconductor microcavities, Phys. Rev. A **90**, 023849 (2014); Y. H. Zhou, H. Z. Shen, and X. X. Yi, Unconventional photon blockade with second-order nonlinearity, *ibid.* **92**, 023838 (2015).
[189] S. Ferretti and D. Gerace, Single-photon nonlinear optics with Kerr-type nanostructured materials, Phys. Rev. B **85**, 033303 (2012).
[190] H. Z. Shen, Y. H. Zhou, and X. X. Yi, Tunable photon blockade in coupled semiconductor cavities, Phys. Rev. A **91**, 063808 (2015).
[191] J. C. Sankey, C. Yang, B. M. Zwickl, A. M. Jayich, and J. G. E. Harris, Strong and tunable nonlinear optomechanical coupling in a low-loss system, Nat. Phys. **6**, 707 (2010).
[192] M. Bhattacharya, H. Uys, and P. Meystre, Optomechanical trapping and cooling of partially reflective mirrors, Phys. Rev. A **77**, 033819 (2008).
[193] J.-Q. Liao and F. Nori, Photon blockade in quadratically coupled optomechanical systems, Phys. Rev. A **88**, 023853 (2013).
[194] H. K. Cheung and C. K. Law, Nonadiabatic optomechanical Hamiltonian of a moving dielectric membrane in a cavity, Phys. Rev. A **84**, 023812 (2011).
[195] U. Weiss, *Quantum Dissipative Systems*, 2nd ed. (World Scientific, Singapore, 1999).
[196] A. O. Caldeira and A. J. Leggett, Quantum tunnelling in a dissipative system, Ann. Phys. (NY) **149**, 374 (1983).
[197] J. Spiechowicz, P. Bialas, and J. Łuczka, Quantum partition of energy for a free Brownian particle: Impact of dissipation, Phys. Rev. A **98**, 052107 (2018).
[198] S. Einsiedler, A. Ketterer, and H.-P. Breuer, Non-Markovianity of quantum Brownian motion, Phys. Rev. A **102**, 022228 (2020).
[199] S. Sinha and P. A. Sreeram, Nonperturbative approach to quantum Brownian motion, Phys. Rev. E **79**, 051111 (2009).
[200] C.-P. Sun and L.-H. Yu, Exact dynamics of a quantum dissipative system in a constant external field, Phys. Rev. A **51**, 1845 (1995).
[201] H. Grabert, P. Schramm, and G.-L. Ingold, Quantum Brownian motion: The functional integral approach, Phys. Rep. **168**, 115 (1988).
[202] A. O. Caldeira and A. J. Leggett, Path integral approach to quantum Brownian motion, Physica A **121**, 587 (1983).